



저작자표시-비영리-변경금지 2.0 대한민국

이용자는 아래의 조건을 따르는 경우에 한하여 자유롭게

- 이 저작물을 복제, 배포, 전송, 전시, 공연 및 방송할 수 있습니다.

다음과 같은 조건을 따라야 합니다:



저작자표시. 귀하는 원저작자를 표시하여야 합니다.



비영리. 귀하는 이 저작물을 영리 목적으로 이용할 수 없습니다.



변경금지. 귀하는 이 저작물을 개작, 변형 또는 가공할 수 없습니다.

- 귀하는, 이 저작물의 재이용이나 배포의 경우, 이 저작물에 적용된 이용허락조건을 명확하게 나타내어야 합니다.
- 저작권자로부터 별도의 허가를 받으면 이러한 조건들은 적용되지 않습니다.

저작권법에 따른 이용자의 권리는 위의 내용에 의하여 영향을 받지 않습니다.

이것은 [이용허락규약\(Legal Code\)](#)을 이해하기 쉽게 요약한 것입니다.

[Disclaimer](#)

공학박사 학위논문

**Polymer/Silica Composites with
Enhanced Mechanical Properties
and Rapid Endothelialization
for Vascular Tissue Engineering**

기계적 특성 및 혈관내피화 속도가 향상된
혈관조직공학용 고분자/실리카 복합체

2021년 08월

서울대학교 대학원

재료공학부

박 수 형

Polymer/Silica Composite with Enhanced Mechanical Properties and Rapid Endothelialization for Vascular Tissue Engineering

지도 교수 김 현 이

이 논문을 공학박사 학위논문으로 제출함
2021년 08월

서울대학교 대학원
재료공학부
박 수 형

박 수 형의 공학박사 학위논문을 인준함
2021년 08월

위 원 장	안 철 희
부위원장	김 현 이
위 원	선 정 윤
위 원	장 태 식
위 원	정 현 도

Abstract

Polymer/Silica Composites with Enhanced Mechanical Properties and Rapid Endothelialization for Vascular Tissue Engineering

Suhyung Park

Department of Materials Science and Engineering

Seoul National University

Biodegradable vascular implants have significant potential to minimize the risks of thrombus formation and arterial restenosis induced from the permanent remaining ones, as resorbed by the surrounding host tissues after a tissue regeneration process. Among various biodegradable materials, polymeric implants have been considered as promising candidates, thanks to their flexibility and availability for easy manufacturing. They, however, exhibit relatively low biocompatibility due to their innate hydrophobicity and hypersensitivity as well as a lack of physical functions such as mechanical

strength or corrosion resistance to be utilized in clinical usage. To overcome these limitations, new composites by introducing bioactive ceramic materials have been studied in terms of material and design, where polymer and ceramic are mutually complementary. Silica, a bioactive ceramic material, hydrolyzed into silicic acid promoting vascular healing and angiogenesis, and also synthesized into diverse morphology by controlling the concentration of silica precursor, reaction time, or ambient pH condition. In this study, we suggested a polymer/silica composite electrospun membrane and coating for artificial vascular graft and magnesium (Mg) vascular stent, respectively, with enhanced biological and physical functions that each application requires.

In the first study, a poly- ϵ -caprolactone (PCL) bilayer vascular graft was fabricated via electrospinning method, composed of an outer layer of randomly-distributed PCL/silica xerogel fibrous membrane and an inner layer of longitudinally-aligned PCL/collagen fibrous membrane. The multilayered structure was to mimic natural human blood vessels so as to withstand dynamic hydraulic stresses and perform great hemocompatibility. In particular, small-diameter vascular grafts (<6 mm) require a suitable mechanical strength, suturability, and anti-thrombogenicity for long-term patency. Here, we synthesized silica xerogel under acid-catalyzed conditions to form nano-skeleton structures through PCL nanofibers of the outer layer, eliciting superior mechanical strength as well as cell-friendly environment. The highly-aligned

structure and materials of the thin inner layer were both favorable for the adhesion, elongation, and migration of endothelial cells, which can lead to rapid re-endothelialization on luminal surfaces of a vascular graft. This electrospun PCL bilayer graft was expected to decrease the possibility of luminal thrombosis and intimal hyperplasia, the main causes for failure in blood vessel transplantation surgery with its rapid endothelial cell coverage and sufficient strength.

In the second study, we incorporated the surface-modified silica nanoparticles (mSiNP) into poly (L-lactic acid) (PLLA) coating for biodegradable Mg stents. Although Mg-based stents possess adequate mechanical properties, non-immunogenicity, and non-toxicity, they degrade explosively under physiological conditions, resulting in clinical stent failure. Polymeric anti-corrosion coating has been adopted on the Mg stents owing to its flexibility to endure considerable deformation during stent expansion, however, conventional PLLA coatings display insufficient corrosion resistance and biocompatibility. For the bifunctional PLLA/mSiNP nanocomposite coatings, the silica nanoparticles were synthesized under base-catalyzed conditions, followed by functionalized with hexadecyltrimethoxysilane (HDTMS), since strong repulsion forces between hydrophobic PLLA and hydrophilic bare silica nanoparticles can cause poor dispersion of the nanofillers. The mSiNPs in the PLLA matrix not only disturbed the penetration

of corrosive medium as a physical barrier, but released silicon ions stimulating endothelial cells as a bioactive material. The nanocomposite coating containing 10 wt% and 20 wt% of the mSiNP delayed the corrosion of the Mg substrate by half and exhibited favorable endothelial cell responses, including initial cell surface coverage, migration, and proliferation rate, compared to the pure PLLA coating.

In conclusion, silica, an inorganic bioactive material, was tailored into a proper morphology by the sol-gel method to form polymer/silica composite so as to accelerate angiogenesis and improve mechanical properties for vascular tissue engineering. The incorporated silica was significantly assured that the dissolved form of silica stimulates both fibroblast and endothelial cells, which, in turn, induced outstanding biological functions. In terms of mechanical properties, the network structure of silica xerogel in the PCL/silica electrospun nanofibrous membrane improved the mechanical strength, and the alkyl-terminated surface of silica nanoparticles in the PLLA/silica nanocomposite coating effectively retarded the degradation rate of the Mg substrate.

Keywords: Vascular tissue engineering; Polymeric implants; Silica; Polymer/silica composite; Nanocomposite; Bioactivity

Student number: 2017-26470

Contents

Abstract	i
List of Tables	vii
List of Figures	viii
Chapter 1. Introduction.....	1
1.1. Biomaterials for vascular tissue engineering.....	2
1.1.1. Vascular artificial graft	3
1.1.2. Intra-arterial stent	4
1.2. Biocompatibility of polymeric vascular implants	6
1.3. Polymer/silica composite scaffold.....	7
1.3.1. Sol-gel derived silica synthesis	8
1.3.2. Bioactivity of silica	9
Chapter 2. PCL/Silica Xerogel Nanofibrous Membrane with Improved Mechanical Strength and Biocompatibility for Artificial Vascular Grafts.....	14
2.1. Introduction.....	15
2.2. Materials and methods	19
2.3. Results and discussion	26
2.4. Conclusion	36

Chapter 3. PCL/Silica Nanocomposite Coating with Enhanced Corrosion Resistance and Biocompatibility for Biodegradable Metal Stents	48
3.1. Introduction.....	49
3.2. Materials and methods	53
3.3. Results	60
3.4. Discussion	69
3.5. Conclusion	77
 Chapter 4. Conclusion.....	 92
 References.....	 95
Abstract (Korean).....	116

List of Tables

Table 1.1. The representative biodegradable implant materials and their mechanical properties.

Table 2.1. Average diameters of PCL/collagen nanofibers collected at rotating speeds of 0, 400, 1,200, and 3,600 rpm.

Table 3.1. Average thickness of pure PLLA and PLLA/mSiNP nanocomposite coatings.

List of Figures

Figure 1.1. (A) Illustration of coronary arterial bypass grafting [35]. (B) Luminal graft recellularization in vivo. The images in a row are stained by haematoxylin and eosin (H&E), Movat's pentachrome, and immunohistochemical method in order from left to right [36].

Figure 1.2. (A) Illustration of coronary artery stenting procedure; a stent is delivered in place using a balloon catheter (a), then, expanded as the balloon inflates (b), and finally implanted as removing the catheter (c) [37]. (B) Luminal endothelialization in vivo. The endothelial cell coverage on each stent was the highest in (d) and the lowest in (b) [38].

Figure 1.3. Schematic illustration of the possible mechanisms of silicate ion in the angiogenic pathway [33].

Figure 2.1. Schematic illustration of the electrospun bilayer vascular graft with an aligned PCL/collagen inner layer and a randomly distributed PCL/silica outer layer.

Figure 2.2. Structural and chemical characterization of pure PCL, PCL/collagen, and PCL/silica electrospun fibers. (A) Representative SEM images (scale bars = 2 μm) of (a) pure PCL, (b) PCL/collagen, and (c) PCL/silica electrospun fibers. (B) Size distributions of the fiber diameters. (C) FT-IR spectra of pure PCL, PCL/collagen, and PCL/silica electrospun nanofibers (\blacklozenge : C=O of amide I; \blacktriangle : N-H of amide II; \bullet : C=O stretching; \bullet : COO vibration; \spadesuit : Si-O-Si bond; \blacktriangledown : Si-OH stretching; \clubsuit : CH₂ stretching). (D) EDS-analyzed chemical compositions of pure PCL and PCL/silica electrospun nanofibers.

Figure 2.3. (A) EDS mapping images of pure PCL and PCL/silica electrospun nanofibers. Red, yellow, and cyan colors represent the elemental distribution of C, O, and Si, respectively. (B) Representative TEM images of a PCL/silica nanofiber (a) before and (b) after burning at 600 $^{\circ}\text{C}$ for 1 h.

Figure 2.4. (A) SEM images (scale bars = 15 μm), (B) FFT frequency spectra, and (C) alignment-angle distributions of PCL/collagen nanofibers electrospun at collector rotation speeds of 0, 400, 1,200, and 3,600 rpm. (D) Peak angle and (E) alignment index of each sample were quantified by FFT analysis (**p < 0.005).

Figure 2.5. (A) Electrospun bilayer vascular graft (length of 2 cm, inner diameter of 3 mm, and wall thickness of 500 μm). Cross-section images of (B) interface between the inner and outer layer, (C) aligned PCL/collagen inner layer, and (D) randomly distributed PCL/silica outer layer.

Figure 2.6. (A) Summary of tensile-stretch mechanical properties of bilayer vascular grafts with PCL or PCL/silica outer layer: UTS, Young's modulus, elongation, and typical stress-strain curves in (a-1 and a-2) longitudinal or (b-1 and b-2) circumferential direction. (B) (a) Suture retention strength and (b) stress-strain curves in longitudinal direction. * $p < 0.05$ and ** $p < 0.01$ vs. the pure PCL group.

Figure 2.7. Cumulative amounts of released Si ions and changes in the ultimate tensile strength of the bilayer vascular graft with the PCL/silica outer layer, as a function of the immersion time.

Figure 2.8. (A) CLSM images of adhered endothelial cells on the PCL/collagen inner layer with a randomly distributed or highly aligned structure (scale bars = 100 μm). Red and blue colors represent actin filaments and cell nuclei, respectively. The arrows in (A) indicate the alignment directions of the nanofibers. (B) Aspect ratios of adhered cells on each inner layer after 1 day of culturing. (C) Viabilities of cells cultured for up to 5 days on each inner layer. Significant differences between the groups are indicated (* $p < 0.05$ and ** $p < 0.01$).

Figure 2.9. (A) CLSM images (scale bars = 400 μm) and (B) relative migration rates of endothelial cells cultured up to 24 h on randomly distributed and aligned PCL/collagen nanofibers. Significant differences between the groups are indicated by ** $p < 0.01$.

Figure 2.10. (A) (a-1 and b-1) Low- and (a-2 and b-2) high-magnified CLSM images of fibroblasts and (B) their spreading areas on pure PCL and PCL/silica outer layers after 1 day of culturing. (C) Viability of cells cultured up to 5 days on each outer layer. * $p < 0.05$ and ** $p < 0.01$ between the groups.

Figure 3.1. (A) Surface morphology of (a) pure PLLA, (b) PLLA/5mSiNP, (c) PLLA/10mSiNP, and (d) PLLA/20mSiNP coating layer on Mg alloy (scale bar = 10 μ m). (B) FT-IR spectra of pure PLLA and PLLA/mSiNP nanocomposite (●: C-H stretching, ■: C=O stretching, ⊙: C-H bending, ◆: C-O stretching, ▲: Si-O-Si stretching, ◆: Si-O-Si bending). (C) Water contact angle measurement on (a) ~ (d). (* $p < 0.05$)

Figure 3.2. (A) SEM images of silica nanoparticles (SiNP) and surface-modified hydrophobic silica nanoparticles (mSiNP). (B) FT-IR spectra of SiNP and mSiNP (●: C-H stretching, ▲: Si-O-Si stretching, ◆: Si-O-Si bending). (C) Water contact angle (WCA) measurement on a slide glass coated with the SiNP and mSiNP (** $p < 0.005$).

Figure 3.3. (A) AFM surface topography of (a) pure PLLA, (b) PLLA/5mSiNP, (c) PLLA/10mSiNP, and (d) PLLA/20mSiNP coating layer on Mg alloy and (B) their measured root mean square roughness (Rq) (* $p < 0.05$ and ** $p < 0.005$).

Figure 3.4. (A) The representative stress–strain curve and (B) summary of mechanical properties of pure PLLA and PLLA/mSiNP nanocomposite films fabricated by solvent-casting method (* $p < 0.05$ and ** $p < 0.005$). (C) Surface morphology of WE43 stent coated with (a) pure PLLA, (b) PLLA/5mSiNP, (c) PLLA/10mSiNP, and (d) PLLA/20mSiNP after the stent expansion process, and their magnified images at the curved part (a') ~ (d') in order.

Figure 3.5. (A) Evolved H_2 gas volume and (B) released Mg ion after immersing Mg alloys coating with pure PLLA, PLLA/5mSiNP, PLLA/10mSiNP, and PLLA/20mSiNP in SBF. (C) Theoretical corrosion rate based on the amount of hydrogen volume (* $p < 0.05$ and ** $p < 0.005$). (D) Si ion release profile tracking after immersing each specimen in SBF solution for

12 days. (E) Surface morphology of (a) pure PLLA, (b) PLLA/5mSiNP, (c) PLLA/10mSiNP, and (d) PLLA/20mSiNP coating layer after 12 days. (F) (a) The representative μ -CT images of pure PLLA-coated and PLLA/10mSiNP-coated Mg stent and (b) their remaining volume change during corrosion test.

Figure 3.6. (A) SEM images of bare Mg plate before and after corrosion test for 12 days. (B) Evolved hydrogen gas volume of bare Mg (non-coated). (C) The pH value of the solution after immersing the bare, PLLA-coated, and PLLA/mSiNP-coated Mg specimens in 40 mL of SBF. (D) The calculation process of theoretical corrosion rate under ideal condition and the resulted value in the case of bare Mg.

Figure 3.7. (A) CLSM images of adhered endothelial cells and (B) their coverage area on (a) pure PLLA, (b) PLLA/5mSiNP, (c) PLLA/10mSiNP, and (d) PLLA/20mSiNP coating layer on Mg alloy substrate after 1 day of culturing. (C) Cell proliferation on each specimen after culturing for 3 days (* $p < 0.05$ and ** $p < 0.005$).

Figure 3.8. (A) Schematic illustration of cell migration test. (B) Cell migration area was calculated over the area of initial cell inhibition zone. (C) CLSM images of endothelial cells on each specimen at 3 and 24 h after removing the barrier (scale bar = 500 μ m).

Figure 3.9. Schematic illustration of bifunctional PLLA/mSiNP nanocomposite coating on the Mg stent surface.

Figure 3.10. (A) (a) XPS full spectra and (b) high resolution spectra of Si 2p for SiNP. (B) (b) XPS full spectra and high resolution spectra of (b') Si 2p and (b'') C 1s for mSiNP. (C) Integrated intensity of each Si 2p peak for SiNP and mSiNP and the relative value was calculated in a bracket.

Figure 3.11. (A) SEM images of the PLLA composite coating containing 10 wt % of (a) bare silica nanoparticles (Si) and (b) surface-modified silica nanoparticles (mSi). (a') and (b') refer a magnified image for (a) and (b), respectively. (B) Tensile stress-strain curve of the PLLA/10Si and PLLS/10mSi film fabricated via solvent-casting method, and (C) their modulus, UTS, and elongation at break. (D) Evolved hydrogen gas volume after immersing PLLA/10SiNP and PLLA/10mSiNP for 12 days.

Figure 3.12. Micro-scratch test on the PLLA and PLLA/mSiNP coatings. (A) Optic images of scratch track on (a) pure PLLA, (b) PLLA/5mSiNP, (c) PLLA/10mSiNP, and (d) PLLA/20mSiNP coating layer and (B) their critical load. (The orange arrows indicate the delamination point)

Chapter 1.
Introduction

1.1. Biomaterials for vascular tissue engineering

Cardiovascular disease is a leading cause of death globally [1]. As the coronary arteries become partially narrow or complete occlusion due to improper intake, smoking, overweight, or chronic diseases, the body lacks nutrients and oxygen, resulting in abnormal physiological activity. Accordingly, several treatment methods to control dynamic molecular interactions associated with inflammation or metabolism have been studied: from pharmaceutical approach to invasive or minimal-invasive surgery with vascular implants [2].

The native human coronary arteries have three layers, which are intima, media, and adventitia, featuring distinct structure and morphology [3]. First, intima, the innermost layer, consists of a monolayer of endothelial cells, which are aligned parallel to the blood stream. Media, the middle layer, contains smooth muscle cells and elastic tissues. Adventitia is the outermost layer, containing fibroblast cells and perivascular nerve cells. The latter two layers maintain the entire blood vessel mechanically from the repeated external stress of heart movement. And the endothelium plays a critical role to prevent thrombosis and intimal hyperplasia, thus, any strategy leading to rapid endothelialization is beneficial for improving clinical patency of vascular implants (**Fig 1.1B** and **Fig 1.2B**).

Biodegradable bio-implants also have potential to reduce the risk from

late-thrombosis, arterial restenosis, long-term immune response induced from the permanent remaining ones, and secondary surgery for removing the inserted implants [4, 5]. Biodegradable vascular implants can be resorbed by the surrounding host tissues after they support or remodel the damaged site by native cells and extracellular matrix (ECM). Representative biodegradable materials are magnesium (Mg) and iron for biometals, hydroxyapatite and tricalcium phosphate for bioceramics, and polyglycolic acid (PGA), poly- ϵ -caprolactone (PCL), and polylactic acid (PLA) for biopolymers [6].

1.1.1. Vascular artificial graft

As plaques accumulates under the luminal area of the blood vessel, blood flow becomes slow, so that the body suffers nutrient and oxygen starvation. Bypass surgeries are necessary to replace the damaged blood vessel with healthy ones, for example, autologous grafts, allografts, and artificial grafts (**Figure 1.1A**) [7]. Artificial grafts have been widely adopted since the others are limited to be supplied, however, the use of small-diameter artificial grafts, the inner diameter of which is smaller than 6 mm, has been rejected due to high risk of clinical failure [3].

The main issues in vascular artificial grafts are over-growth of smooth muscle cells, thrombosis, and abnormal dilation or contraction caused by

mechanical mismatch [8]. Therefore, biocompatibility (or bioactivity) is a primary requirement for the artificial grafts to be integrated with the adjacent blood vessels while maintaining the entire structure during the recovery period, about several weeks. In this regard, the nanofibrous membrane fabricated by electrospinning method provides high mechanical and biological properties, as mimicking the fibrillary structure of the natural ECM [9-11]. Adjusting the material and structure of the membrane is also facile, because various materials, including the seeded cells, can be ejected in a proper morphology by controlling the conditions, such as fiber diameter, porosity, and fiber alignment.

1.1.2. Intra-arterial stent

Stent is an inserted device for structurally supporting narrowed or weakened blood vessels to prevent occlusion and intimal hyperplasia. In clinical situation, stents are often mounted and cramped on a balloon catheter, which expands at the implantation site (**Figure 1.2A**). As stent can reduce the inflammation or any risk during percutaneous transluminal coronary angioplasty in less-invasive way, it has been widely used in cardiovascular field [12]. The first generation was bare metal stents, made of stainless steel, chromo-cobalt alloys or nickel titanium, however, they

faced high risks of restenosis, so the next generations are drug-eluting and biodegradable stents. The main concerns related to the vascular stent field are stent fracture/collapse, incomplete endothelialization and the following hyperplasia and thrombosis, and hypersensitivity caused by the materials or drug. To accomplish the required properties, the ideal stents should possess proper mechanical strength for preventing stent recoil or failure as well as outstanding biocompatibility for rapid revascularization [13].

The commercially-available biodegradable stents are poly-L-lactic acid (PLLA) stents and Mg alloy stents [14]. The mechanical and biological properties of PLLA are inferior to them of Mg due to relatively low strength and innate hydrophobicity. Mg alloy stents exhibits sufficient radial force, but its corrosion resistance needs to be improved, because excessive amount of hydrogen gas production may block or disturb blood flow to induce blood clotting, and fast alkalization is also able to cause inflammatory response [15, 16]. Various surface treatments such as chemical modification or physical coating retard the degradation rate of Mg, sustaining its instinct properties. Among them, polymeric coating has been widely adopted for biodegradable stents due to its flexible and deformable property, while ceramic coating, based on calcium phosphate or silicon carbide, is vulnerable to external deformation [17].

1.2. Biocompatibility of polymeric vascular implants

Polymeric materials have already been utilized in various tissue engineering applications because their mechanical properties (**Table 1.1**), especially flexibility, are similar to natural tissues, and the chemical and morphological properties are also susceptible to be modified [18, 19]. In the vascular tissue engineering field, for instance, expanded polytetrafluoroethylene (ePTFE) membranes are commercial artificial vascular grafts due to their high mechanical strength and porous structure, but their low biocompatibility and non-biodegradability could evoke acute thrombosis, inflammation, or neointimal thickening for small diameter grafts [20, 21]. Thus, many studies are based on biodegradable polymers, which are classified into two types: natural polymers (e.g. chitosan, collagen, alginate, and silk) and synthetic polymers (e.g. PGA, PCL, and PLA). Natural polymers generally exhibit great biocompatibility, presenting receptor-binding ligands to cells, but insufficient mechanical property, low purity, and short-term degradation should be developed. Although biodegradable synthetic polymers overcome many limitations that the natural polymers undergo, their poor biocompatibility and hemocompatibility with innate hydrophobicity still brings out foreign body reaction in the immune system [19].

1.3. Polymer/silica composite scaffold

The ideal vascular implants require several factors, including biocompatibility, proper degradation rate, and specific physical functions. Considering synthetic polymers lack the biological cues to provide functional sites for biomolecules, polymer blends with natural or other synthetic polymers, polymer/bioceramic composites, and surface modification have been studied to increase affinity with the host tissues [22]. In particular, polymer/silica composite scaffolds not only showed high biocompatibility and bioactivity to promote cellular response and tissue regeneration as they stimulate biological functions but increased mechanical properties by creating a chemical bond between the silanol end groups on the silica surface and the organic polymer chains [23].

Polymer/silica composites can be fabricated by simple mixing, in-situ polymerization, or sol-gel method [24]. Simple mixing is mixing the silica nanoparticles with the polymer, and in this case, uniform distribution of the particles in the polymer matrix is crucial. In-situ polymerization occurs after blending the as-prepared silica nanoparticles and the monomers. Sol-gel method is a process where silica particles are synthesized from silica precursor.

1.3.1. Sol-gel derived silica synthesis

In the sol-gel process, the precursor, mainly silicon alkoxide Si(OR)_4 , reacts through continuous hydrolysis and condensation to synthesize silica SiO_2 . The reaction is relatively very slow under neutral pH, therefore, acid or base catalysts are necessary to initiate the reaction, where the Si-OR is hydrolyzed to Si-OH , which is capable to form siloxane bonds, resulting from dehydration condensation with another Si-OR or Si-OH [25-27]. In acid-catalyzed sols, the hydrolysis is dominant to deprotonate only the end of the polysilicates, while the deprotonation of silanol groups is deactivated. Thus, cluster-cluster aggregation occurs preferentially, eventually organizing into polymer-like network structure. In base-catalyzed sols, however, deprotonation is facile so that hydrolyzed monomers are condensed with each other, thus, monomer-cluster aggregation mainly occurs. As a result, particle-like highly branched structure can be obtained [28]. Besides, the structure, size, porosity, and induced function of silica depend on the reaction condition, including above-mentioned pH, temperature, concentration of reagent, and surfactant [27].

1.3.2. Bioactivity of silica

Silica is a biodegradable ceramic material, which is hydrolyzed into silicic acid molecules (Si(OH)_4) under physiological environment; both silica and its byproduct are approved as a safe bioavailable material by US-FDA [29-31]. The biodegradation of silica depends on the physical/chemical properties of the material itself, like the surface functionality, pore size, and crystallinity, or the properties of the ambient media, like the pH, temperature, and media flow status. The exact chemical structure of the byproducts and its bioactivity mechanism are uncertain, however, it has been demonstrated that silica-based biomaterials accelerate angiogenesis by stimulating endothelial progenitor cell homing, migration, differentiation, and tubular formation [32]. As depicted in **Figure. 1.3**, the dissolved form of silica in the body has been reported to induce a hypoxic condition by inhibiting prolyl hydroxylase domain (PHD2) enzyme, so as to activate hypoxia-induced factor-1 (HIF-1). To be specific, the released ions from the silica stabilize and accumulate HIF-1 α in the cytosol of fibroblast or endothelial cells, which forms an HIF-1 complex in the nucleus with HIF-1 β . The HIF-1, then, activates the hypoxia response element, regulating the expression of vascular endothelial growth factor (VEGF) to promote neovascularization and tissue regeneration [32, 33].

Polymer	Tg (°C)	Tm (°C)	Modulus (GPa)	Strength (MPa)	Elongation at break (%)	Degradation (months)
PLA	60	180–190	2–4	65	2–6	18–30
PDLLA	55	Amorph	1–3.5	40	1–2	3–4
PLLA	60–65	175	2–4	60–70	2–6	>24
PGA	35–40	225–230	6–7	90–110	1–2	4–6
PDLGA (50/50)	45	Amorph	1–4.3	45	1–4	1–2
PLGA (82/12)	50	135–145	3.3–3.5	65	2–6	12–18
PCL	-54	55–60	0.34–0.36	23	>4,000	24–36
PLA/PCL (70/30)	20	100–125	0.02–0.04	2–4.5	>100	12–24
PC	~147	225	2–2.4	55–75	80–150	>14
WE43 (Mg alloy)	N/A	540–640	40–50	220–330	2–20	3–12
SS 316L	N/A	1,371–1,399	193	668	40	Biostable
Co-Cr	N/A	~1,454	210	235	40	Biostable

PLA, polylactic acid; PDLLA, poly-DL-lactic acid; PLLA, poly-L-lactic acid; PDLGA, poly-DL-lactide-co-glycolide; PGA, polyglycolide; PLGA, poly-lactic-co-glycolide; PCL, polycaprolactone; PLA/PCL, polylactic acid/polycaprolactone; Mg, magnesium; SS, stainless steel; Co-Cr, cobalt chromium.

Table 2.1. The representative biodegradable implant materials and their mechanical properties [34].

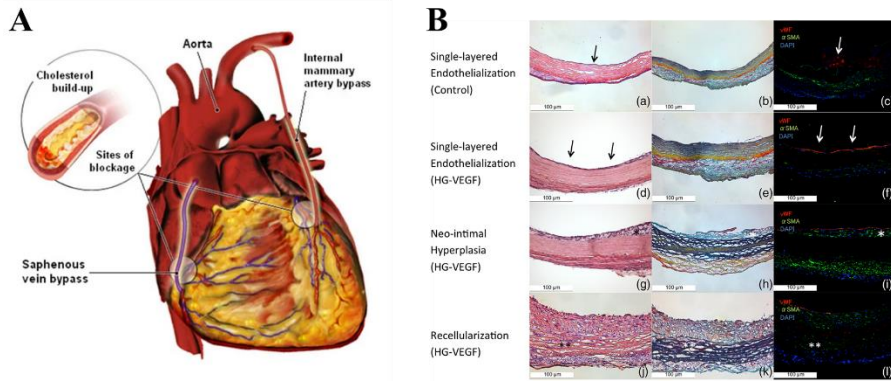


Figure 1.1. (A) Illustration of coronary arterial bypass grafting [35]. (B) Luminal graft recellularization *in vivo*. The images in a row are stained by haematoxylin and eosin (H&E), Movat's pentachrome, and immunohistochemical method in order from left to right [36].

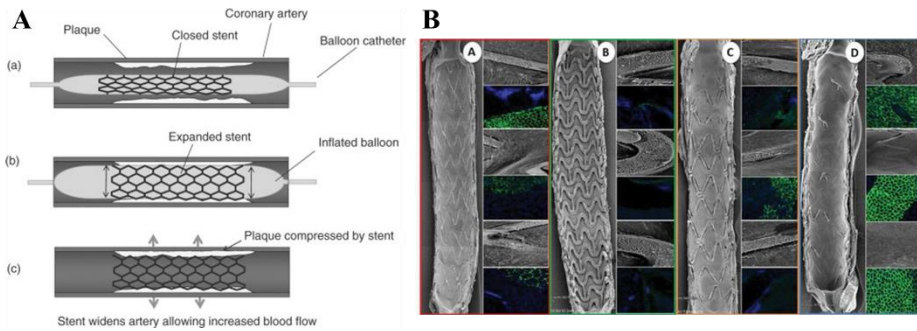


Figure 1.2. (A) Illustration of coronary artery stenting procedure; a stent is delivered in place using a balloon catheter (a), then, expanded as the balloon inflates (b), and finally implanted as removing the catheter (c) [37]. (B) Luminal endothelialization *in vivo*. The endothelial cell coverage on each stent was the highest in (d) and the lowest in (b) [38].

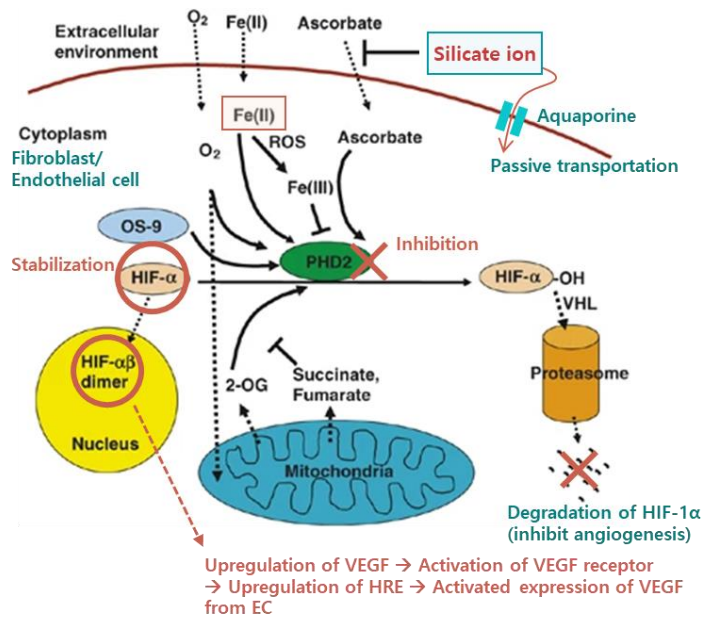


Figure 1.3. Schematic illustration of the possible mechanisms of silicate ion in the angiogenic pathway [33].

Chapter 2.

PCL/Silica Xerogel Nanofibrous Membrane with Improved Mechanical Strength and Biocompatibility for Artificial Vascular Grafts

2.1. Introduction

Synthetic, artificial vascular grafts are considered to be essential biomedical implants for replacement or bypassing an entire section of a damaged blood vessel. They have proved advantageous owing to flexibility in their shape, length, and diameter, with unlimited availability and consistent quality; this allows the use of artificial vascular grafts in diverse practical settings [39, 40]. Most commercially available artificial vascular grafts developed to date are composed of non-biodegradable materials, such as expanded polytetrafluoroethylene, polyurethane, and polyethylene terephthalate. Their unique advantages of chemical stability, long-term robustness, and non-toxicity facilitate the successful replacement of large-diameter blood vessels [41]. However, when used for small-diameter blood vessels, the currently available artificial vascular grafts often fail to meet the requirements of microvascular surgery because of unfavorable biological responses, including delayed re-endothelialization, surface thrombosis, and neointimal hyperplasia [9, 42].

To overcome these limitations, the development of new combinations of materials and designs that elicit a favorable healing process and enable gradual degradation and complete replacement by normal vessels has received substantial attention in recent years. In particular, rapid formation of the endothelial cell monolayer on the luminal surface of the vascular graft provides

an anti-thrombogenic characteristic and minimizes hemodynamic disturbances in the graft [43, 44]. Therefore, the emerging field of vascular graft engineering focuses on biocompatible materials and structural designs that promote cell adhesion, spreading, and proliferation on the graft surfaces [45-47]. Electrospun poly- ϵ -caprolactone (PCL) nanofibers have shown high adaptability and the potential to provide excellent biomechanical features (e.g., desired flexibility, porosity, and biodegradability) and structural similarity with the fibrillary structure of the extracellular matrix of blood vessels [48-50]. Moreover, the alignment of electrospun PCL nanofibers provides nano-scale topographical cues as a guidance for endothelial cell elongation and migration, which play critical roles in the maturation and biological functionality of natural blood vessels [51, 52]. In this regard, considerable efforts have been devoted to designing and fabricating novel PCL vascular grafts with unique mechanical and biological functions. For example, a bilayer PCL vascular graft was fabricated with different nanofiber orientations in the inner and outer layers [53]. The inner layer consisted of nanofibers that were longitudinally aligned via two parallel metal strip collectors to facilitate endothelial cell adhesion and alignment, whereas the outer layer was randomly oriented to improve cell motility through the scaffold thickness. Another PCL-based bilayer vascular graft was composed of an inner layer of randomly oriented PCL nanofibers and an outer layer of circumferentially aligned poly(lactic acid) nanofibers, prepared using a rotating collector [54]. This bilayer structure provided

sufficient radial strength and compliance-matching with neighboring arteries. However, PCL is characterized by innate hydrophobicity, poor cellular activity, and hypersensitivity to plasma proteins; therefore, the introduction of bioactive polymers (e.g., silk, chitosan, collagen, or hyaluronic acid) as a coating or blending material is often required to overcome these disadvantages of PCL [45, 55, 56]. Among these polymers, collagen, one of the most common components in natural blood vessels, has shown remarkable improvements in the cellular affinity and anti-inflammatory activity of electrospun PCL [55, 57]. However, most studies have focused on the compositional functionality with respect to biological aspects, which cannot satisfy the complex requirements for mechanical properties needed in practical settings.

Previously, we explored whether the biomechanical properties and cellular responses of PCL can be ameliorated by hybridization with bioceramics [58-60]. In particular, we demonstrated that sol-gel-derived silica possessed excellent wettability and bioactivity and was relatively easy to incorporate into a polymeric substance, without any segregation or phase separation [61, 62]. These unique characteristics made it possible to develop uniform electrospun PCL/silica nanofibers with substantially improved mechanical strength, hydrophilicity, and cellular affinity [62]. Hence, in this study, we designed a novel small-diameter vascular graft with a bilayer tubular structure, consisting of a thin inner layer composed of longitudinally aligned PCL/collagen

nanofibers and a relatively thick outer layer composed of a PCL/silica hybrid with randomly distributed nanofibers. We then investigated the morphological, chemical, and mechanical properties of the fabricated bilayer vascular graft, as well as the in vitro affinity for endothelial and fibroblast cells.

2.2. Materials and methods

2.2.1. Materials

PCL ($M_n = 80,000$); tetramethylorthosilane (TMOS); hydrochloric acid (1 M); 1,1,1,3,3,3-hexafluoro-2-propanol (HFP); and all other reagents were purchased from Sigma–Aldrich (St. Louis, MO, USA), except for collagen, which was obtained from SK Bioland (Chungnam, Korea).

2.2.2. Preparation of a bilayer vascular graft via electrospinning

To electrospin solutions for the PCL/collagen inner layer and the PCL/silica outer layer, the weight percentages of collagen and silica were fixed at 20%, based on a previous study [62, 63]. The PCL/collagen solution was prepared by dissolving 10 g of PCL and 2.5 g of collagen in 100 mL of an HFP solution, with overnight stirring. For the PCL/silica solution, a silica–sol was obtained by mixing TMOS, deionized water, HCl, and HFP at a volume ratio of 5:1:0.02:4. After 1 h of stirring to obtain a single-phase sol, the calculated amount of the silica sol was added to a PCL solution (20 g of PCL dissolved in 100 mL of HFP) to obtain a final weight ratio of 80:20 for PCL and silica [62].

The electrospinning setup consisted of a high-voltage power supply, a syringe pump, and two types of in-house grounded collectors (e.g., plate- and

drum-shaped). The prepared solutions were loaded in 5-mL plastic syringes (NanoNC Co., Korea) and injected through 20-gauge blunt-end metal needles at a constant flow rate of 0.2 mL/h (for PCL/collagen) or 1.0 mL/h (for PCL/silica). When fabricating the inner and outer layers, the distance between the needle tip and the collector was fixed at 15 cm, and the applied voltage was set to 15 kV. Aligned PCL/collagen nanofibers for the inner layer were generated by electrospinning onto a rotating mandrel collector at a speed of up to 3,600 rpm. Then, the electrospun-fabricated inner layer was carefully detached from the collector and wrapped in a longitudinal direction around a small-diameter rod (diameter = 3 mm). Subsequently, randomly distributed PCL/silica nanofibers were deposited on the PCL/collagen inner layer without rotating the rod. The total thickness of the bilayer vascular graft was fixed at 500 μm . Then, the electrospun-fabricated bilayer was carefully detached from the collector and stored in a vacuum desiccator for up to 2 days to eliminate the residual HFP solvent. To stabilize collagen within the inner layer, a further chemical-crosslinking treatment was performed with 100 mM 1-ethyl-3-(3-dimethylaminopropyl) carbodiimide and 25 mM *N*-hydroxysuccinimide in 70% ethanol for 24 h.

2.2.3. Characterization of vascular grafts

The surface morphology of the electrospun nanofibers was characterized using scanning electron microscopy (SEM; JSM-6360, JEOL, Japan) with an accelerating voltage of 20 kV. The distribution of the fiber diameters was determined by measuring at least 100 individual fibers in the SEM images. Fast Fourier transform (FFT) analysis was used to evaluate the degree of alignment of the PCL/collagen nanofibers in the SEM images [64]. The FFT algorithm converted the SEM image of electrospun nanofibers into a frequency spectrum, based on the pixel intensity, and then the intensity was quantified by determining radial sums along the various angles using ImageJ software (National Institutes of Health, USA). The highest-intensity angle was expressed as the peak angle, and an alignment index was calculated according to the fraction of alignment intensities within 5° of the peak angle to the same fraction of a theoretically randomized state (i.e., $10^\circ/180^\circ \approx 0.0556$) [65, 66].

The chemical compositions of the electrospun PCL/collagen and PCL/silica nanofibers were characterized by Fourier transform-infrared spectroscopy (FT-IR; Nicolet 6700, Thermo Scientific, USA) over a range of 4,000 to 500 cm^{-1} , using 64 scans. Additionally, the distribution of silica in the electrospun nanofibers was further examined using an energy-dispersive X-ray spectroscopy (EDS) system integrated with the SEM.

2.2.4. Mechanical testing

The longitudinal elastic modulus, tensile strength, and suture retention strength (SRS) of the bilayer vascular grafts were measured and compared using a tensile-strength instrument (Model 5565; Instron Corp., Danvers, MA, USA) at a constant extension speed of 5 mm/min. The grafts were hydrated in phosphate-buffered saline (PBS) at room temperature before mechanical testing. At least four samples of each membrane were measured. The electrospun bilayers were cut into rectangles with a length of 40 mm and a width of 10 mm. For samples with an aligned PCL/collagen inner layer, the stretching direction was parallel to the direction of alignment. The thickness of each membrane was measured using a micrometer to calculate the cross-sectional area, and the membrane was clamped with an inter-clamp distance of 20 mm. The ultimate tensile strength (UTS) and elongation at the point of breaking were obtained by generating a strain–stress curve.

For the suture retention test, membranes were cut into rectangles with a dimension of 10 × 50 mm ($n = 4$). The bottom end was fixed, and a 4-0 polyglycolic acid monofilament suture thread (AV 434 needle; Ailee Co., Busan, Korea) was passed through a hole 2 mm from the top end of the membrane. The suture loop was extended at a controlled speed of 2 mm/min until the membrane was entirely ripped. The SRS was defined as the maximum force measured during the test, implying the resistance of vascular grafts to pulling out the

sutures.

2.2.5. Si ion release

Electrospun bilayer samples with the PCL/silica outer layer were prepared at a size of 10 mm × 10 mm and immersed in 10 mL PBS (Welgene, Inc., Korea) for 7 days at 37°C. Half of the solution was collected every 24 h to analyze the concentration of the released Si ions using an inductively coupled plasma mass spectrometer (NexION 350D, PerkinElmer, USA) and replaced with 5 mL of fresh PBS. After the concentration of Si was saturated, the tensile strengths of the bilayer samples were investigated and compared with the initial value (before immersion).

2.2.6. *In vitro* cellular assays

In vitro cellular responses of bilayer vascular grafts were evaluated in terms of the attachment of human umbilical vein endothelial cells (HUVECs; American Type Culture Collection [ATCC], CRL-1730) and mouse fibroblast cells (L929; ATCC, CCL-1) to investigate the biocompatibility of the inner and outer layers, respectively. All membranes were immersed in ethanol for 3 h and sterilized by ultraviolet irradiation on a clean bench for 1 h before seeding the cells. HUVECs and fibroblast cells were seeded on the inner and outer layers,

respectively, followed by incubation in a humidified incubator in an atmosphere containing 5% CO₂ in air at 37°C. HUVECs were cultured in endothelial cell basal medium-2 (Lonza, Walkersville, MD, USA) supplemented with 5% fetal bovine serum and 1% penicillin–streptomycin, and fibroblasts were cultured in α -minimum essential medium (Welgene Co., Korea) supplemented with 10% fetal bovine serum and 1% penicillin–streptomycin.

For confocal laser scanning microscopy (CLSM; FluoView FV1000, Olympus Co., Ltd., Japan), cells were treated with Alexa Fluor® 55-conjugated phalloidin (Invitrogen, Carlsbad, CA, USA) and ProLong® Gold antifade reagent with 4,6-diamidino-2-phenylindole (Invitrogen) to stain the cytoplasm and nucleus, respectively. The cell-spreading area was calculated using the ImageJ measurement tool, and the aspect ratio of elongated cells along PCL/collagen fibers was also examined for HUVECs.

For the adhesion test, the cell density was 5×10^4 cells/mL for both the inner and outer layers, and for the migration test, the cell density was 10×10^4 cells/mL on the inner layer, with cells cultured for 24 h in both cases. To monitor cell migration along random and aligned nanofibrous inner layers, a cell-inhibition zone was formed by placing a block on each sample after seeding the cells. The block was removed after the cells sufficiently covered the surface, and the cell medium was replaced with fresh medium to remove cells remaining in the original medium. The samples were incubated at 5% CO₂ and 37°C, and

stained with green-fluorescent calcein AM (Thermo Scientific, MA, USA) to observe the migration distances of live cells at 0, 3, and 24 h.

Cell proliferation was evaluated using a methoxyphenyl tetrazolium salt assay with 3-(4,5-dimethylthiazol-2-yl)-5-(3-carboxymethoxyphenyl)-2-(4-sulfophenyl)-2*H*-tetrazolium (Promega, Madison, WI, USA) at cell densities of 1×10^4 and 2×10^4 cells/mL on the inner and outer membranes, respectively ($n = 3$). After 3 or 5 days of incubation, all samples were washed with PBS, transferred to new tissue culture plates, immersed in fresh medium with the tetrazolium compound dye, and incubated at 37°C for 2 h. The quantity of formazan product formed as a result of the mitochondrial activity in live cells was measured as the absorbance at 492 nm, using a microplate reader (Model 550; Bio-Rad).

2.2.7. Statistical analysis

All quantitative values were statistically analyzed using the Statistical Package for the Social Sciences program (International Business Machines, NY, USA) and are presented as the mean \pm standard deviation. The significance of differences was examined using the Shapiro–Wilk test, followed by one-way analysis of variance, with a p-value set at < 0.05 .

2.3. Results and discussion

In this study, we designed a novel small-diameter vascular graft with a bilayer tubular structure, consisting of a thin inner layer composed of longitudinally aligned PCL/collagen nanofibers, which may act as topographical and chemical cues for rapid endothelialization on the luminal surface, and a relatively thick outer layer composed of a PCL/silica hybrid with randomly distributed nanofibers, which may provide a sufficient mechanical strength and satisfactory biocompatibility (**Figure 2.1**).

2.3.1. Surface characterization of electrospun PCL/collagen and PCL/silica

To investigate the surface morphology, electrospun PCL/collagen and PCL/silica fibers were examined by SEM, as shown in **Figure 2.2Aa–c**. Pure PCL was also observed for comparison purposes. All samples showed homogeneous and continuous nanofibrous structures without any beads or noticeable defects, and their fiber diameters fell in the range of 50–700 nm (**Figure 2.2B**). The average diameters were 204 ± 89 , 358 ± 92 , and 239 ± 86 nm for pure PCL, PCL/collagen, and PCL/silica, respectively, without any significant differences. The chemical compositions of the electrospun PCL/collagen and PCL/silica fibers were confirmed by FT-IR and EDS analyses, as shown in **Figure 2.2C&D**. Both samples clearly presented bare

PCL characteristic peaks for CH₂ stretching, C=O stretching, CH₂ bending, and COO vibrations [62]. In addition, we also exhibited specific peaks of the incorporated collagen and silica. For PCL/collagen, the specific peaks of collagen are shown at 1,650 and 1,536 cm⁻¹ for the C=O group of the amide linkage (amide I) and the N-H bonds of the amide (amide II), respectively. For PCL/silica, Si-O-Si bonds and Si-OH-stretching vibrations are shown at 1,065 and 785 cm⁻¹ and at 935 cm⁻¹, respectively [62, 67]. The EDS and elemental-mapping results confirmed the presence of silica in electrospun PCL/silica fibers (**Figure 2.3A**); approximately 7% of the silica was uniformly distributed throughout the whole nanofibrous structure, indicating that the silica was successfully incorporated into the PCL nanofiber matrix via the sol-gel method and was uniformly distributed at a nanoscale.

2.3.2. Fabrication of an inner layer with aligned PCL/collagen nanofibers

The first step in fabricating the bilayer vascular graft was to generate an aligned PCL/collagen inner layer by introducing a high-speed rotating collector as the receiving device. The rotational movement of the collector can drive the mechanical stretching force needed for aligning the electrospun nanofibers [68]. Thus, the alignment degrees of PCL/collagen nanofibers were examined by varying the collector rotation speed from 400 to 3,600 rpm.

As shown in **Figure 2.4A**, all samples exhibited uniform and continuous surface morphologies with no breakage in length or irregularity in shape. The measured average diameters of the nanofibers showed a slightly decreasing tendency with increased rotation speeds (**Table 2.1**); however, no statistically significant differences were observed among the samples. In addition, the micrographs clearly show that the nanofibers were deposited on the collector with different degrees of alignment as follows: randomly distributed (0 and 400 rpm), slightly aligned (1,200 rpm), and highly aligned (3,600 rpm) nanofibers. FFT analysis also indicated that the degree of fiber alignment increased with increased rotation speeds of the collector. While the PCL/collagen nanofibers formed without rotation showed a symmetrical circular distribution of grayscale pixels in the FFT-output spectrum, the grayscale pixels became distributed asymmetrically, in an elliptical shape, as the rotation speed of the collector increased (**Figure 2.4B**). Further, oval-plot profile analysis was performed on the FFT spectra, wherein the radial intensity of the grayscale pixels was summed and plotted against the acquired angle. As shown in **Figure 2.4C**, only the PCL/collagen nanofibers prepared at 1,200 and 3,600 rpm showed characteristic peaks of aligned fibers, with a high intensity and a relatively small area under the curve. In particular, when the rotation speed was 3,600 rpm, the electrospun PCL/collagen nanofibers exhibited the narrowest peaks at an angle of 92° , with the smallest peak-angle distribution and the maximum alignment-index value of 2.4, indicating the highest degree

of fiber alignment. These results clearly demonstrated that the PCL/collagen nanofibers prepared at 3,600 rpm had a high potential as topographic cues for guiding endothelial cell alignment and endothelialization on the surface.

2.3.3. Evaluation of mechanical properties and degradability of the bilayer vascular graft

A high mechanical strength and elastic modulus in the longitudinal and circumferential directions are essential for practical applications with vascular grafts because they must withstand repeated mechanical stresses such as expansion, shrinkage, bending, and stretching in the in vivo environment, due to the blood pressure and bodily movements [69]. Moreover, when implanted into natural blood vessels during surgery, vascular grafts require sufficient handling stability and suturability in order to sustain the forces of stitching during surgical procedures [70].

Pure PCL or PCL/silica was electrospun with a random fiber orientation and deposited on the prepared aligned PCL/collagen inner layer with a constant thickness. Each inner PCL/collagen layer and outer PCL/silica layer were fixed at a thickness of 150 and 350 μm , respectively, so that the thickness of the entire fabricated bilayer graft was maintained at 500 μm (**Figure 2.5**), which was similar to that of the native coronary arterial wall [71,

72]. The tensile properties of the fabricated bilayer vascular grafts were measured in the longitudinal and circumferential directions, and the Young's modulus, ultimate tensile strengths, elongations at break, and typical stress–strain curves are represented in **Figure 2.6A**. The pure PCL outer layer provided good flexibility and stretchability to the vascular graft, which exhibited an elongation of more than 150% at break in the longitudinal direction and 130% in the circumferential direction. However, its other mechanical properties, when compared with those of the human coronary artery (UTS: 1.5–6.3 MPa and Young's modulus: 4.5–23.87 MPa [3, 70]), did not qualify the graft for use in a vascular graft application. In contrast, the PCL/silica outer layer remarkably enhanced the mechanical properties of the vascular graft, which showed 260% and 215% higher UTS and Young's modulus values in the longitudinal direction and 220% and 395% higher values in the circumferential direction, respectively, than those of the pure PCL graft (**Figure 2.6Aa&b**). In addition, unlike the substantially reduced Young's modulus of the pure PCL graft in the circumferential direction compared with that in the longitudinal direction, no significant mechanical difference was observed with the PCL/silica outer layer in the longitudinal and circumferential tensile tests. The level of elongation at break (69% and 70% in the longitudinal and circumferential directions, respectively) was somewhat lower in the graft with the PCL/silica outer layer than in that with the pure PCL outer layer, but this value was much closer to that of the native coronary artery (45–99%) [70],

indicating a positive impact of silica incorporation into the PCL outer layer on graft mechanical properties, which better matched those of the human arterial system. Previously, we confirmed that a sol–gel-derived silica xerogel readily formed uniform nanostructures in an organic matrix and provided superior mechanical properties [61, 62]. As shown in **Figure 2.3B**, the PCL/silica nanofibers clearly formed mesoporous nano-skeleton structures in PCL nanofibers, which should be beneficial for inducing mechanical interlocking between the rigid silica phase and the flexible PCL matrix, making the graft more suitable for vascular applications.

In addition, the SRS (i.e., the material strength required to resist a pull-out load or tearing during suturing the graft to the artery) of the vascular graft with the PCL/silica outer layer was much greater than that of the graft with the pure PCL outer layer (2.70 ± 0.46 and 0.93 ± 0.10 MPa, respectively) (**Figure 2.6B**). For successful implantation and long-term patency of a vascular graft, sufficient SRS, exceeding the threshold value of 2.0 N, is generally required [73]. Unfortunately, the pure PCL outer layer failed to provide sufficient mechanical support because of its innate low stiffness and mechanical strength. These direct comparisons of the mechanical properties of the bilayer vascular grafts with the pure PCL or PCL/silica outer layer clearly showed positive effects of silica incorporation into the PCL nanofiber matrix on the mechanical properties and suturability of the graft.

Sol-gel-derived silica is well known for its rapid dissolution characteristics. Thus, a mechanical test was also performed on a vascular graft with the PCL/silica outer layer, which was immersed in PBS at 37°C for up to 5 days. As shown in **Figure 2.7**, because of the initial burst release of the incorporated silica, the cumulative amount of Si ions rapidly increased on day 1; however, the rate of release subsequently decreased, approaching a steady-state and sustained-release profile by day 5, which was very similar to the data from previous studies [61, 62]. It was also noticed that as Si ions were released, the tensile strength of the vascular graft showed the opposite tendency, such that the initial UTS gradually decreased to 2.53 ± 0.82 MPa on incubation day 5. However, this vascular graft was significantly stronger than that with the pure PCL outer layer, and its mechanical properties were still within the range of values considered acceptable for clinical use [3, 70].

2.3.4. *In vitro* endothelial cell behavior on the PCL/collagen inner layer

To investigate the ability of the aligned PCL/collagen inner layer to promote endothelialization and improve the anti-thrombogenicity of small-diameter vascular grafts, the adhesion morphology, migration rate, and proliferation degree of HUVECs were closely examined as a function of the culture time. PCL/collagen with randomly distributed nanofibers was tested as a control to assess the effect of structural alignment on HUVEC responses. As

shown in **Figure 2.8A**, the adhered cells were significantly elongated along the underlying aligned nanofibers and formed a monolayer over time on the aligned electrospun fibers, whereas cells on randomly distributed nanofibers displayed a polygonal, irregular appearance with a relatively small spreading area and low cell numbers. Quantitative analysis of the adhered cells after 1 day of culture also indicated that the aspect ratio (the highest length-to-width ratio) of the cells on the aligned PCL/collagen nanofibers was almost twice as high as that of the cells on the randomly distributed PCL/collagen nanofibers (**Figure 2.8B**). Furthermore, cells on the aligned nanofibers displayed higher levels of cell viability for up to 5 days of culture than did those on the randomly distributed nanofibers, and the difference between the two groups increased as the incubation time increased (**Figure 2.8C**).

To directly compare randomly arranged and aligned PCL/collagen nanofibers in terms of their ability to support cell migration, a cell-free gap of approximately 700 μm in width was formed within the cell monolayers of both samples, which served as a cell-migration niche. As shown in **Figure 2.9A**, both samples clearly supported endothelial cell migration toward the center, and the gap gradually decreased over time. However, a significant difference was found between the samples in terms of the relative migration distance. After 3 h of cell culturing on the aligned fibers, the gap decreased by almost 50%, and a 100% cell-migration ratio was reached after 24 h, whereas the gap reduction on

the randomly oriented fibers was only 20% or 40% after 3 or 24 h of incubation, respectively (**Figure 2.9B**). These results clearly indicated that the aligned PCL/collagen nanofiber structure provided important topological cues to improve the directional migration of adhered cells (parallel to the fiber orientation) and to increase the cell-proliferation rate. In general, aligned-surface structures at a nanometer scale highly restrict the formation of lateral protrusions of adhered cells because of the dimensional manipulation of cell-adhesion sites. Therefore, it is possible for cells along the aligned direction of the surface structure to exhibit a highly stretched morphology and progressive motility. Furthermore, it has been reported that the metabolic activity of endothelial cells can be upregulated by coherent and unidirectional signaling between adjacent cells, resulting in enhanced rates of proliferation and cell-surface coverage [74]. Because endothelial cells release anticoagulation factors that prevent platelet attachment and activation [75], our results suggest that the aligned PCL/collagen nanofiber structure should alleviate thrombus formation and prevent complete occlusion after graft implantation.

2.3.5. *In vitro* fibroblast cell behavior on the PCL/silica outer layer

In the outermost layer of natural blood vessels, fibroblast cells are primarily distributed within a collagenous matrix and play important roles in maintaining the vascular tone by regulating nitric oxide (NO) activity.

Adventitial fibroblasts generate extracellular superoxide, which can inactivate NO via direct catalysis to form its oxidation product (NO_3). Therefore, we investigated the vascular graft remoldability via fibroblast adhesion and proliferation on its outer layer. As shown in **Figure 2.10A**, the pure PCL outer layer showed only a few cells, which were individually adhered to the surface, retained their spherical shape, and showed little or no spreading behavior. In contrast, the PCL/silica outer layer showed noticeably enhanced fibroblast adhesion, with a large number of cells attached to its surface, active filopodia formation, and a significantly larger spreading area (**Figure 2.10B**). Quantitative cell-proliferation results also reflected favorable responses of fibroblasts cultured on the PCL/silica layer (**Figure 2.10C**). During 5 days of culturing, the cell-viability values on the PCL/silica outer layer were significantly greater than those on pure PCL, and the differences became more pronounced as the culturing time increased. Our previous studies on polymer–silica composites demonstrated that incorporating a silica component into the polymer matrix directly stimulated fibroblast adhesion and proliferation via the excellent surface hydrophilicity of silica and upregulation of the metabolic activity of fibroblasts [76-78]. Because highly proliferating fibroblasts synthesize and secrete collagen, fibronectin, and glycosaminoglycan, fibrous connective tissue can be rapidly formed on the PCL/silica outer layer; therefore, the bilayer vascular graft may achieve long-term clinical safety and desired long-term outcomes in patients [79, 80].

2.4. Conclusion

In summary, we successfully fabricated a new PCL-based bilayer vascular graft with a rapid endothelialization capability and strong mechanical properties by controlling the structure and material composition of each layer. The thin inner layer of aligned PCL/collagen nanofibers allowed endothelial cells to adhere and rapidly migrate, thus enabling rapid endothelialization of the luminal surface of the vascular graft. The relatively thick outer layer of randomly distributed PCL/silica nanofibers provided superior mechanical properties and supported satisfactory affinity of fibroblasts. Overall, this report describes a simple and affordable fabrication process, combining material composition and structural changes and resulting in the assembly of a small-diameter vascular graft with a promising clinical potential for vascular tissue engineering.

Fiber diameter (nm) of PCL/collagen composite membranes electrospun on a drum collector rotating at each speed (rpm)	
0	357.59 ± 91.76
400	310.67 ± 33.64
1200	305.93 ± 33.75
3600	297.41 ± 85.47

Table 2.1. Average diameters of PCL/collagen nanofibers collected at rotating speeds of 0, 400, 1,200, and 3,600 rpm.

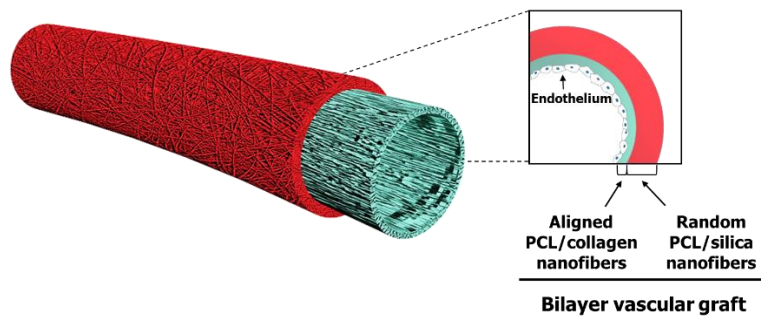


Figure 2.1. Schematic illustration of the electrospun bilayer vascular graft with an aligned PCL/collagen inner layer and a randomly distributed PCL/silica outer layer.

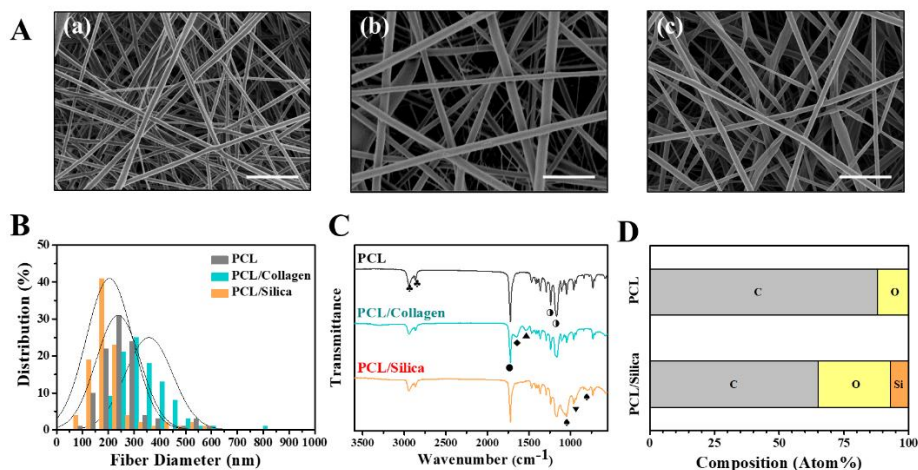


Figure 2.2. Structural and chemical characterization of pure PCL, PCL/collagen, and PCL/silica electrospun fibers. (A) Representative SEM images (scale bars = 2 μm) of (a) pure PCL, (b) PCL/collagen, and (c) PCL/silica electrospun fibers. (B) Size distributions of the fiber diameters. (C) FT-IR spectra of pure PCL, PCL/collagen, and PCL/silica electrospun nanofibers (\blacklozenge : C=O of amide I; \blacktriangle : N-H of amide II; \bullet : C=O stretching; \bigcirc : COO vibration; \spadesuit : Si-O-Si bond; \blacktriangledown : Si-OH stretching; \clubsuit : CH_2 stretching). (D) EDS-analyzed chemical compositions of pure PCL and PCL/silica electrospun nanofibers.

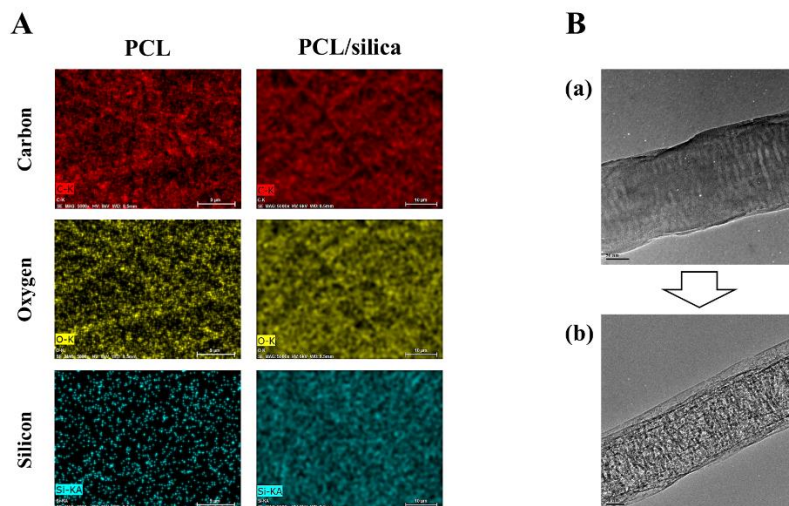


Figure 2.3. (A) EDS mapping images of pure PCL and PCL/silica electrospun nanofibers. Red, yellow, and cyan colors represent the elemental distribution of C, O, and Si, respectively. (B) Representative TEM images of a PCL/silica nanofiber (a) before and (b) after burning at 600 °C for 1 h.

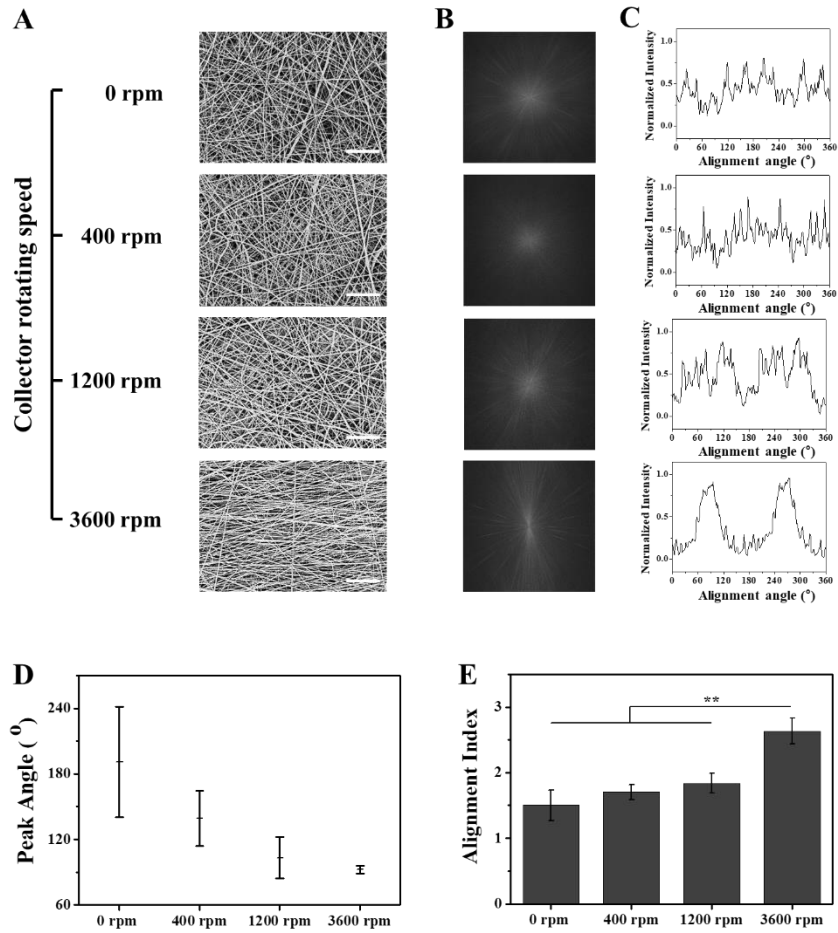


Figure 2.4. (A) SEM images (scale bars = 15 μm), (B) FFT frequency spectra, and (C) alignment-angle distributions of PCL/collagen nanofibers electrospun at collector rotation speeds of 0, 400, 1,200, and 3,600 rpm. (D) Peak angle and (E) alignment index of each sample were quantified by FFT analysis (** $p < 0.005$).

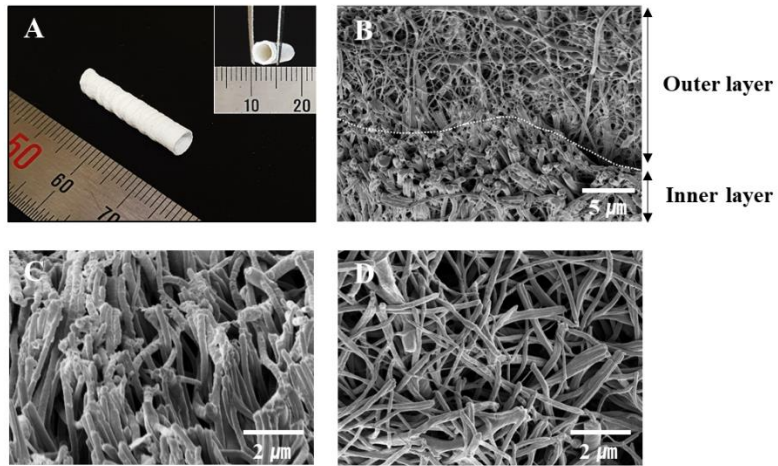


Figure 2.5. (A) Electrospun bilayer vascular graft (length of 2 cm, inner diameter of 3 mm, and wall thickness of 500 μm). Cross-section images of (B) interface between the inner and outer layer, (C) aligned PCL/collagen inner layer, and (D) randomly distributed PCL/silica outer layer.

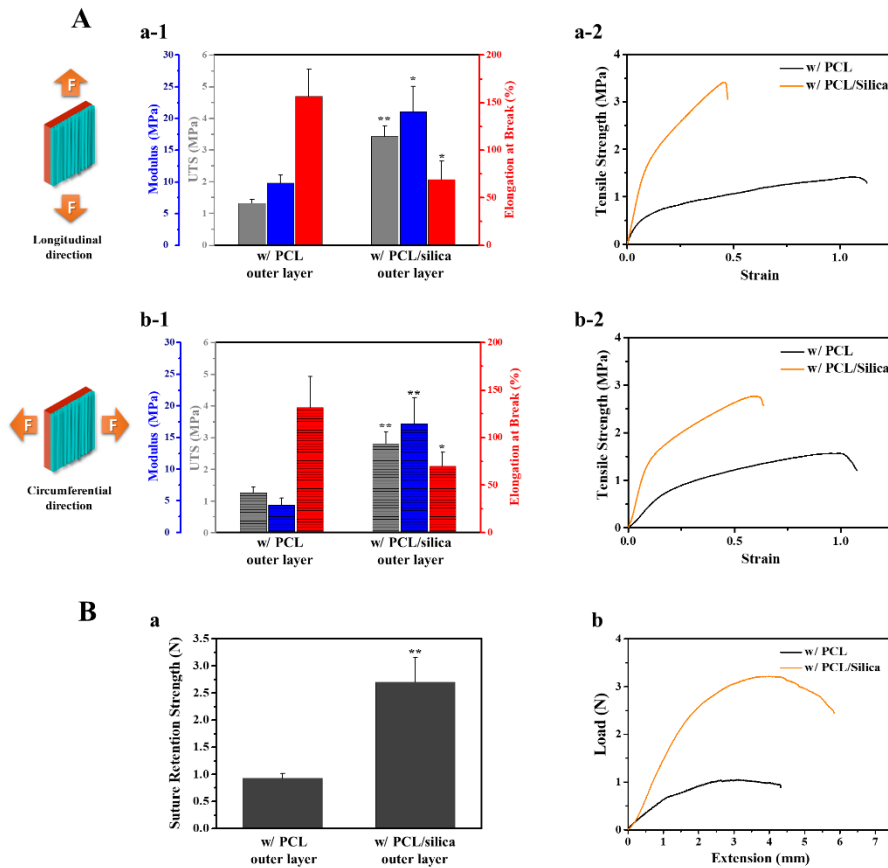


Figure 2.6. (A) Summary of tensile-stretch mechanical properties of bilayer vascular grafts with PCL or PCL/silica outer layer: UTS, Young's modulus, elongation, and typical stress-strain curves in (a-1 and a-2) longitudinal or (b-1 and b-2) circumferential direction. (B) (a) Suture retention strength and (b) stress-strain curves in longitudinal direction. * $p < 0.05$ and ** $p < 0.01$ vs. the pure PCL group.

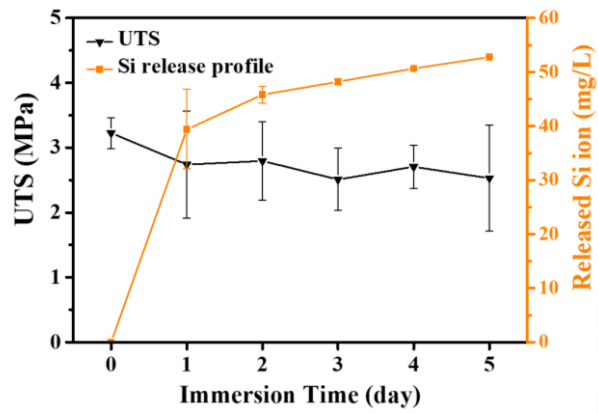


Figure 2.7. Cumulative amounts of released Si ions and changes in the ultimate tensile strength of the bilayer vascular graft with the PCL/silica outer layer, as a function of the immersion time.

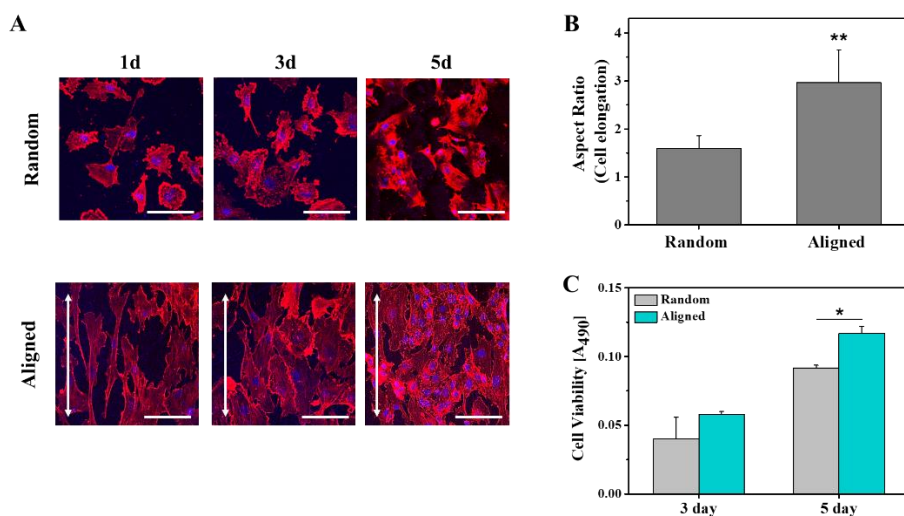


Figure 2.8. (A) CLSM images of adhered endothelial cells on the PCL/collagen inner layer with a randomly distributed or highly aligned structure (scale bars = 100 μm). Red and blue colors represent actin filaments and cell nuclei, respectively. The arrows in (A) indicate the alignment directions of the nanofibers. (B) Aspect ratios of adhered cells on each inner layer after 1 day of culturing. (C) Viabilities of cells cultured for up to 5 days on each inner layer. Significant differences between the groups are indicated (* $p < 0.05$ and ** $p < 0.01$).

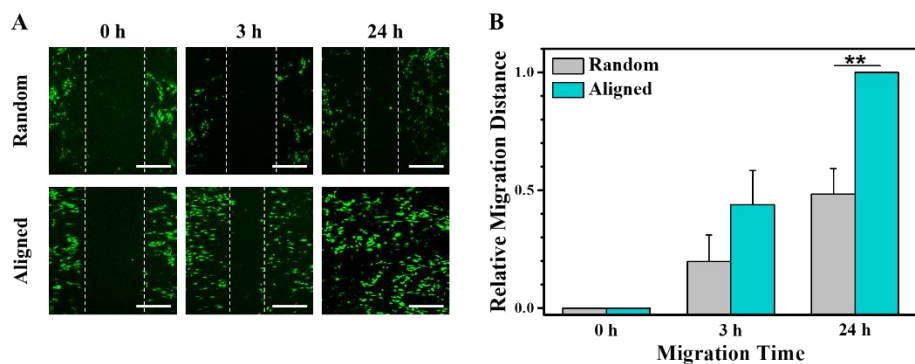


Figure 2.9. (A) CLSM images (scale bars = 400 μm) and (B) relative migration rates of endothelial cells cultured up to 24 h on randomly distributed and aligned PCL/collagen nanofibers. Significant differences between the groups are indicated by ** $p < 0.01$.

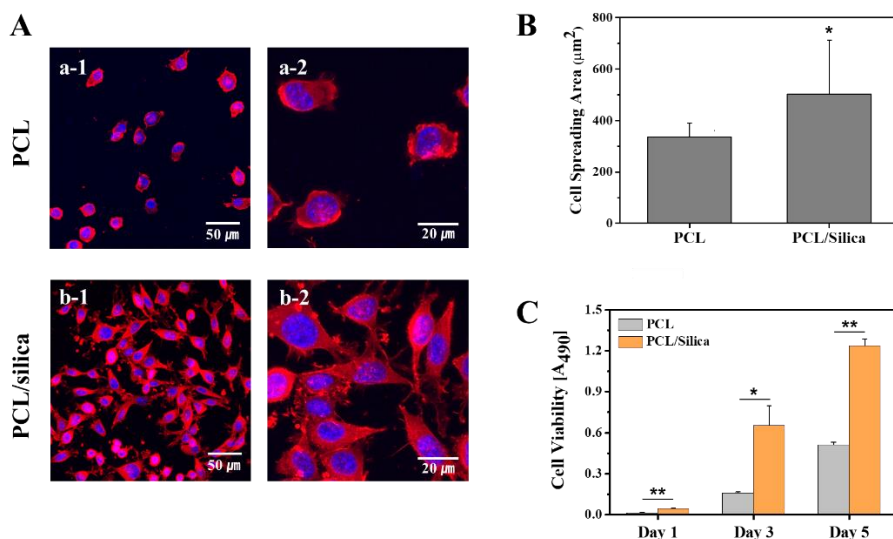


Figure 2.10. (A) (a-1 and b-1) Low- and (a-2 and b-2) high-magnified CLSM images of fibroblasts and (B) their spreading areas on pure PCL and PCL/silica outer layers after 1 day of culturing. (C) Viability of cells cultured up to 5 days on each outer layer. * $p < 0.05$ and ** $p < 0.01$ between the groups.

Chapter 3.

PCL/Silica Nanocomposite Coating with

Enhanced Corrosion Resistance and

Biocompatibility for Biodegradable Metal Stents

3.1. Introduction

Cardiovascular disease is a leading cause of severe disability and death, and its incidence has been steadily increasing worldwide [81]. When coronary arteries become narrow due to the deposition of lipids and cholesterol, pernicious symptoms such as angina, heart failure, and heart attack arise due to abnormal blood circulation [82]. Percutaneous intervention, known as coronary stenting, is a promising treatment for solving these problems; in this approach, a balloon-assisted or self-expanding stent is deployed at the target lesion with minimally invasive bypass surgery and to promote blood vessel patency [82, 83]. Among the various types of stents, metallic stents, generally fabricated from cobalt-chrome alloys or nickel-titanium alloys, possess high elastic moduli, expandability, and flexibility, leading to their preferential use in clinical practice [82, 84]. However, several studies revealed that these metallic stents remain permanently within the blood vessels of patients and increase the potential risks of late in-stent restenosis, thrombosis, local inflammation, and prolonged physical irritation after stent implantation [85-87]. Therefore, biodegradable stents have attracted significant attention, as they can provide temporary mechanical support to the inner vessel wall during the healing period and then disappear progressively [83].

Magnesium (Mg)-based stents are the first commercially released biodegradable metallic stents, signifying their inherent high mechanical

properties, non-immunogenicity, and non-toxicity to the human body compared to polymeric biodegradable stents [83, 86, 88-90]. In addition, Mg ions are reported to be essential for endothelial cell activity and function while possessing low thrombogenicity and antiarrhythmic characteristics, which can prevent platelet activation on the surface as well as abnormal microvessel contraction [91, 92]. However, Mg-based stents have an extremely high corrosion rate under physiological conditions; therefore, there is a high risk of unexpected structural collapse and stent failure during clinical service. Although Mg is well-known for its biocompatibility, the generation of excessive degradation byproducts, such as $\text{Mg}(\text{OH})_2$ and hydrogen gas, may lead to local tissue alkalization and hydrogen bubble formation, thereby impairing vascular tissue remodeling [83, 93, 94].

To address these issues, considerable efforts have been devoted to enhancing the corrosion resistance of Mg stents, and introducing polymeric coating layers on the Mg surface has been demonstrated as effective for stent applications because of its high elasticity during stent deployment and good coatability even on complex-shaped stents [83, 95]. Several biodegradable polymers, such as poly (L-lactic acid) (PLLA), polycaprolactone, and poly (lactic-co-glycolic acid), have demonstrated acceptable biocompatibility and FDA approval status for use in stent applications. As they play a role in promoting the physical barrier function on the surface of Mg, it is possible to

achieve stable corrosion protection ability for the Mg stent by increasing the coating thickness [83, 96-98]. However, as the polymeric coating possesses inherently high mechanical mismatch with the Mg stent, the increased coating thickness may not endure stable coating deformations during the stent deployment process, thereby resulting in crack formation and partial or full delamination of the coating layers [99]. Moreover, most synthetic biodegradable polymers exhibit poor vascular tissue responses, showing delayed re-endothelialization, long-term thrombosis, and inflammatory reactions [100, 101]. Thus, the coating of the Mg stent is desired to protect it from rapid corrosion and reduce biological risks while retaining a functional thickness.

Recently, silica (SiO_2) has been proposed as a nanoparticle for polymer-based nanocomposites owing to its various functionalities by modifying its surface chemistry [102-105]. In addition, silica is well known for its biodegradability and excellent endothelial cell affinity. It can be hydrolyzed into silicic acid (Si(OH)_4) to be excreted through the urine, which has reported as no cytotoxicity within a concentration range of $0.0625 \sim 400 \mu\text{g/ml}$ [30].

The dissolved form of silica induces a hypoxic condition by mimicking the metallic ions that inactivates prolyl hydroxylase domain (PHD2) enzyme to activate hypoxia-induced factor-1 (HIF-1), which regulates the expression of vascular endothelial growth factor (VEGF) [32, 33], therefore, they are

considered beneficial for promoting vascular healing and regeneration around stents [106, 107]. Regarding corrosion protection, it is possible to decrease the rate of water penetration into the polymer coating layer by incorporating hydrophobic silica nanoparticles into the polymer matrix [108]. This hydrophobic surface modification can also hinder the nanoparticles aggregate in the relatively hydrophobic polymer matrix, displaying homogeneous dispersion, which induces robust biological functions by stimulating the specific cells or bacteria continuously as well as promoted mechanical strength by regulating the mobility of polymer chains [109, 110]. However, despite these advantages, there has been no attempts to apply silica to biodegradable polymer coatings for Mg stents. In this study, we selected PLLA as a representative biodegradable polymeric coating material because it has been extensively utilized for Mg surface coating and fabricated a PLLA/silica nanocomposite coating on the surface of the Mg stent. To ensure sufficient corrosion protection, the surface of silica nanoparticles was modified to be hydrophobic (mSiNP), and the physical, chemical, and mechanical properties, corrosion protection ability, degradation behavior, and *in vitro* endothelial cell affinity of the nanocomposite coating with different weight ratios of the mSiNPs were examined in comparison with those of the pure PLLA coating.

3.2. Materials and methods

3.2.1. Materials

Mg alloy WE43 (4.1 wt% yttrium, 2.1 wt% neodymium, 0.56 wt% zirconium, 0.028 wt% manganese, Yueyang Yuhua Yejin Company, China) was manufactured into a plate and stent specimen as substrate. Poly-L-lactic acid granules (99.9%, $M_n = 60,000\text{--}80,000$) was provided by Pureco (Korea). Tetraethyl orthosilicate (TEOS), dichloromethane (DCM), ammonium hydroxide solution (28.0–30.0%, NH_4OH), hexadecyltrimethoxysilane (HDTMS), and other reagents were purchased from Sigma-Aldrich Corporation (USA).

3.2.2. Sample preparation

Silica nanoparticles (SiNPs) were synthesized using the Stöber method [111]. First, 50 mL of ethanol, 3 mL of TEOS, and 3 mL of ammonium hydroxide were stirred vigorously for 2 h at 50 °C. Subsequently, 0.51 mL of HDTMS was added and reacted for 15 min to modify the surface of the silica particles to induce hydrophobicity. The modified silica nanoparticles (mSiNP) were obtained by centrifugation (10,000 rpm, 5 min), rinsed with ethanol, centrifuged repeatedly, and then dried in an oven at 70 °C. For the PLLA/mSiNP nanocomposite coating, the as-prepared mSiNPs were sonicated

in DCM to allow uniform dispersion, after which 10 w/v% of PLLA granules were dissolved in the silica suspension. The ratios of mSiNP to PLLA were 0, 5, 10, and 20 wt%, named PLLA, PLLA/5mSiNP, PLLA/10mSiNP, and PLLA/20mSiNP, respectively. Each coating solution was spin-coated on the WE43 alloy specimens (10 mm × 10 mm × 2 mm) at 3000 rpm for 1 min and then polished with SiC abrasive papers up to 2000 grit, followed by washing with ethanol to remove grease.

3.2.3. Characterizations of PLLA/mSiNP nanocomposite coating layer

The surface morphology of the PLLA/mSiNP nanocomposite coating layers was observed using field-emission scanning electron microscopy (FE-SEM; SUPRA 55VP, Zeiss, Germany) with an accelerating voltage of 20 kV. Their chemical compositions were characterized by Fourier-transform infrared spectroscopy (FT-IR; Nicolet iS50, Thermo Fisher Scientific, USA) from 400 to 4000 cm⁻¹. To evaluate the wettability of each coating layer, a 3.0 µl droplet of distilled water was formed on the surface, and its image was captured to fit in a circular shape and measured using a water contact angle analyzer (WCA; SmartDrop, Femtobiomeb, Korea). The surface roughness was compared after investigating three regions of each specimen with an area of 30 µm × 30 µm by atomic force microscopy (AFM; NANO Station II, Surface Imaging Systems, Germany).

3.2.4. Coating stability test

The WE43 coronary stent, with an inner diameter of 3 mm and length of 20 mm, was coated with four concentrations of PLLA/mSiNP solution (0, 5, 10, and 20 wt% mSiNP to PLLA) to confirm coating stability during stent expansion. The stents were prepared in a crimped state, with a diameter of 1.8 mm, followed by electrochemical and ultrasonic polishing processes in ethanol. The as-prepared coating solution was sprayed on a rotating Mg alloy stent substrate under controlled solution flow rate, substrate speed, nozzle and substrate distance, and air pressure conditions. The PLLA/mSiNP-coated stents were then mounted on a balloon catheter filled with distilled water, expanding until the inner diameter reached 3 mm by increasing the water pressure gently up to 12 atm. The surface morphology was examined to assess the coating stability of the Mg stent by FE-SEM.

Additionally, the PLLA/mSiNP films were fabricated by solvent casting for tensile testing using a universal testing machine (UTM; Model 5565, Instron Corp., Danvers, USA) to compare the mechanical strength with the silica particle content. The solution was prepared in the same manner as the above-mentioned spin-coating solution, poured into Petri dishes, and dried slowly. After 48 h to allow enough time for the organic solvent to evaporate thoroughly, they were cut into a 50 mm long and 10 mm wide rectangle. The as-prepared tensile test specimens were clamped with a gauge length of 15 mm

and extended at a constant speed of 3 mm/min. The thickness was gently measured using a micrometer to obtain a cross-sectional area for the generation of a stress–strain curve.

3.2.5. Corrosion test

The corrosion behavior of the PLLA/mSiNP-coated magnesium alloy specimens was compared by measuring the amount of evolved hydrogen gas during magnesium degradation. The bottom and sides of all samples were protected with epoxy so that only the top (10 mm × 10 mm) was exposed. Four as-prepared samples for each experimental group (PLLA, PLLA/5mSiNP, PLLA/10mSiNP, and PLLA/20mSiNP) were immersed in 100 mL of simulated body fluid (SBF) for 12 days at 37 °C, and the resultant hydrogen gas was collected by the water substitution method. After 12 days of *in vitro* corrosion tests in a physiological environment, they were gently washed with ethanol and dried to observe the surface morphology of the coating layer by FE-SEM.

On the basis of the coating stability and corrosion protection ability, the pure PLLA and PLLA/10mSiNP nanocomposite coatings were selected for the evaluation of the Mg stent degradations. The PLLA- and PLLA/10mSiNP-coated Mg stents were tightly placed into the silicone tube by a balloon-assisted expansion under SBF immersion condition at 37 °C. The degradation behavior

of Mg stents was monitored by micro-computed tomography (μ -CT; Skyscan 1173, Bruker, USA) operating at a voltage of 130 kV and current of 60 μ A at a prescribed time. Their remaining volume and 3D morphology were analyzed using commercial softwares, CTAn and CTVox, from Bruker.

3.2.6. Mg and Si ion release test

The epoxy-protected PLLA/mSiNP specimens at an exposed area of 10 mm \times 10 mm were immersed in 5 mL of SBF solution to monitor the concentration of released Mg and silicon (Si) ions from each sample for 12 days at 37 °C by inductively coupled plasma atomic emission spectrometry (ICP-AES; Optima-4300DV, PerkinElmer, USA). The solution was collected for evaluation at 2, 4, 8, and 12 days after immersion and replaced with fresh SBF. The Mg ion release profile was further compared to the corrosion behavior, as they were positively correlated.

3.2.7. *In vitro* biocompatibility test

The *in vitro* cellular behaviors of PLLA/mSiNP-coated WE43 specimens were evaluated using human umbilical vein endothelial cells (HUVECs; CRL-1730, American Type Culture Collection) to analyze the effect

of incorporating silica nanoparticles into the coating layer in terms of adhesion, proliferation, and migration. All samples were sterilized by immersion in 100% ethanol for 3 h, followed by exposure to UV irradiation for 1 h.

For the initial adhesion and proliferation test, HUVECs were seeded on the four different specimens at a density of 3×10^4 cells/mL in endothelial cell basal medium-2 (Lonza, Walkersville, USA) supplemented with 5% fetal bovine serum and 1% penicillin–streptomycin and then cultured in a humidified incubator containing 5% CO₂ at 37 °C. After culturing for 1 d, the cells were stained with green fluorescent calcein AM (Thermo Scientific, USA) for confocal laser scanning microscopy (CLSM; SP8X, Leica, Germany). The cell spreading morphology and coverage area of each specimen were observed and calculated quantitatively using the ImageJ threshold tool. To evaluate cell viability, the samples were obtained after 3 d of incubation, washed with PBS, transferred to a new cell culture plate immersed in fresh medium containing 10% Cell Counting Kit-8 reagent (CCK-8; Dojindo Laboratories, Japan), and incubated for 2 h. The optical absorbance originating from the formazan product was measured at a wavelength of 450 nm using a microplate reader (Victor 3, Perkin Elmer, USA).

The migration of HUVECs was monitored after they sufficiently covered the entire surface, excluding a cell inhibition zone where a rubber block had been placed on each specimen. All samples were gently washed with PBS,

and the adhered cells were incubated in a fresh cell medium at 5% CO₂ at 37 °C. Their migration distance was observed via CLSM at 0, 3, and 24 h after the block was removed.

3.2.8. Statistical analysis

All evaluations were conducted using at least three samples per group. The measured values were reported as the mean \pm standard deviation and were statistically analyzed using the Social Sciences program (SPSS 23, SPSS Inc., USA). Normality was investigated using the Shapiro–Wilk test, and the statistical significance of differences was evaluated by one-way analysis of variance (ANOVA) based on a p-value below 0.05.

3.3. Results

3.3.1. Surface characterizations of PLLA/mSiNP nanocomposite coating

The surface morphology, chemical properties, wettability, and surface roughness of the PLLA/mSiNP nanocomposite coating layers with different amounts of mSiNP were investigated using SEM observation, FT-IR analysis, water contact angle (WCA) measurement, and AFM analysis. As a control group, the Mg specimens coated with pure PLLA were also analyzed using the same method. In the case of the PLLA/mSiNP nanocomposite coatings (**Figure 3.1Ab–d**), incorporated silica nanoparticles clearly appeared on the surface of coatings with sub-micron-sized aggregation, while the pure PLLA coating only showed a smooth and flat surface morphology (**Figure 3.1Aa**). All coated Mg samples showed no defects or pinholes on their surfaces. According to the supplementary data, the thickness of the coatings was within a range of 3.12–3.96 μm (**Table 3.1**). In the FT-IR spectra (**Figure 3.1B**), the characteristic peaks of PLLA were detected on both pure PLLA and PLLA/mSiNP nanocomposite coatings at 2997 and 2946 cm^{-1} for C–H stretching, 1747 cm^{-1} for C=O stretching, 1454, 1382, and 1359 cm^{-1} for C–H bending, and 1180, 1129, and 1081 cm^{-1} for C–O stretching [61]. In addition, the PLLA/mSiNP nanocomposite coating exhibited additional peaks at 1050 and 792 cm^{-1} for Si–O–Si stretching and 440 cm^{-1} for Si–O–Si bending, compared to the pure PLLA coating [61]. According to the supplementary data (**Figure 3.2**), characteristic

peaks of hydrophobic silica nanoparticles (C–H stretching at 2923 and 2850 cm^{-1}) overlapped with neighboring PLLA peaks. The wettability of the pure PLLA and PLLA/mSiNP nanocomposite coatings were determined at different mSiNP amounts using WCA measurements, as shown in **Figure 3.1C**. The water droplet maintained its round shape on the pure PLLA coating with an average WCA of 71° . As the mSiNP amount increased, the WCA also increased up to 77° with a statistically significant difference ($P < 0.05$) when 10 and 20 wt% of mSiNPs were incorporated into the PLLA coating.

AFM surface 3D topography (**Figure 3.3A**) confirmed that the incorporation of mSiNP substantially increased the surface roughness of the coating compared to that of pure PLLA; the smooth and flat surface of pure PLLA was changed to exhibit rough and uneven surface morphology with only 5 wt% of mSiNP incorporation (**Figure 3.3Aa–b**). This trend becomes more severe with increasing amounts of mSiNP, and in the case of the PLLA/20mSiNP coating, there is almost no flat region on the surface profiles with numerous observable nanoscale pits (**Figure 3.3Ac&d**). The statistical measurement of root mean square surface roughness, R_q , also represented continuously increased average surface roughness value of coatings with increasing amount of mSiNP, showing 22.7 ± 4.07 , 40.2 ± 3.21 , 50.2 ± 2.19 , and 58.1 ± 2.85 nm of average surface roughness for pure PLLA, PLLA/5mSiNP, PLLA/10mSiNP, and PLLA/20mSiNP coatings, respectively.

3.3.2. Mechanical stability of PLLA/mSiNP nanocomposite coatings

The mechanical properties of the pure PLLA and PLLA/mSiNP nanocomposites were preliminarily examined by applying a tensile load without the Mg substrate. For this test, each specimen was fabricated in a film shape using the solvent casting method. **Figure 3.4A** depicts the typical stress–strain curves of the films with different mSiNP amounts, and the elastic modulus, ultimate tensile stress (UTS), and strain-to-failure are shown in **Figure 3.4B**. As expected, the typical ductile fracture behavior of pure PLLA was converted to brittle fracture as the amount of mSiNP increased. Notably, with 10 wt% of mSiNP, the elastic modulus and UTS reached the highest values among all samples, showing 1.84 ± 0.184 GPa and 36.6 ± 3.22 MPa, respectively, which is 64% and 61% higher than those of pure PLLA (elastic modulus: 1.12 ± 0.166 GPa, UTS: 22.8 ± 1.48 MPa). However, the further addition of 20 wt% mSiNP did not result in any additional improvement in the mechanical properties, rather than resulting in a slight reduction in both the elastic modulus and UTS (elastic modulus: 1.63 ± 0.073 GPa, UTS: 30.9 ± 2.40 MPa).

To investigate the practical coating stability, each coating layer was formed on the Mg stent via spray-coating, and after the balloon-assisted stent expansion process, their surface morphologies were observed using SEM. As shown in **Figure 3.4C**, pure PLLA and its nanocomposite coatings with up to

10 wt% mSiNP uniformly covered the entire surface of the Mg stents with uniform and flawless surface morphologies (**Figure 3.4Ca–c**). Even in the magnified images at the corner segments of the stent-strut, there was no noticeable damage or defect on the coatings, and they only exhibited a very smooth and continuous coating surface (**Figure 3.4Ca'–c'**). However, in the case of the PLLA/20mSiNP coating, considerable coating cracks were observed at the corner segment (**Figure 3.4Cd**), and the bare Mg surface was partially exposed through cracks in the high-magnification image (**Figure 3.4Cd'**).

3.3.3. Degradation behaviors

The corrosion protection ability of pure PLLA and PLLA/mSiNP nanocomposite coatings was evaluated by measuring the evolved hydrogen gas volume and the amount of Mg ions released from each coated Mg substrate under SBF immersion for 12 days (**Figure 3.5A–C**). According to the supplementary data (**Figure 3.6A&B**), the bare Mg sample exhibited massive evolution of H₂ gas during the entire immersion period; after 12 days of immersion, the thick and rough corrosion products were fully covered over the surface of the Mg sample. In the case of the pure PLLA coating, it suppressed the initial burst evolution of H₂ gas for up to 3 days of immersion. However, after that time, its corrosion protection was not sufficient, exhibiting a rapid increase in H₂ gas volume for up to 12 days of immersion. In contrast, when the

mSiNP was incorporated into the PLLA, the coating layer exhibited enhanced corrosion protection ability compared to pure PLLA, and noticeably, PLLA/10mSiNP and PLLA/20mSiNP coatings exhibited substantially less H₂ gas volume, reaching only 1.5 and 2 mL after 12 days of immersion, and the pure PLLA-coated Mg reached 8.4 mL at the same time point (**Figure 3.5A**). The Mg ion release test results also showed good agreement with the H₂ gas evolution test results. The pure PLLA coating showed the highest rate of Mg ion release during the entire immersion period, and with increasing mSiNP amount, the rate becomes significantly slower than that of the pure PLLA coating. In particular, in the case of the PLLA/10mSiNP and PLLA/20mSiNP coatings, the values of released Mg ions at 12 days of immersion were approximately 40% lower than those of the pure PLLA coating (**Figure 3.5B**). **Figure 3.5C** depicts the theoretical corrosion rate, calculated based on the total H₂ gas volume during the SBF immersion test, using the chemical reaction equation: $\text{Mg(s)} + 2\text{H}_2\text{O(l)} \rightarrow \text{Mg(OH)}_2\text{(aq)} + \text{H}_2\text{(g)} \uparrow$ (**Figure 3.6D**). The corrosion rate significantly decreased as mSiNPs were incorporated into the PLLA matrix, which was 0.623 ± 0.168 , 0.356 ± 0.051 , and 0.245 ± 0.084 mm/year for PLLA/5mSiNP, PLLA/10mSiNP, and PLLA/20mSiNP, respectively, whereas pure PLLA-coated Mg corroded at a rate of 1.41 ± 0.453 mm/year.

The degradation of mSiNP in the coatings was also monitored by

measuring the amount of Si ions released from the coating during the same immersion period (**Figure 3.5D**). As expected, the results indicate that all nanocomposite coatings exhibited a gradual degradation of mSiNP in the PLLA coating matrix, and the total amount of Si ions was proportional to the amount of incorporated mSiNP in the PLLA. The highest number of ions (8.64 ± 0.752 mg/L) was observed in the PLLA/20mSiNP coating, whereas 3.17 ± 0.244 and 2.67 ± 0.817 mg/L of Si ions were detected on the PLLA/10mSiNP and PLLA/5mSiNP coatings, respectively.

After 12 days of immersion, the surface morphology of each coating was observed using SEM, as shown in **Figure 3.5E**. The pure PLLA coating showed a substantial coating fracture with severely torn and delaminated coating edges, where the bare Mg surface was largely exposed to the SBF solution. In the case of the PLLA/5mSiNP coating, a noticeable localized coating failure with crack formation and partial delamination was observed, but it displayed a much smaller area of exposed Mg substrate than pure PLLA coating. In contrast, the PLLA/10mSiNP and PLLA/20mSiNP coatings almost possessed their original coating morphologies, and only a few micro-sized cracks appeared on their surfaces without any noticeable coating delamination or Mg substrate exposure.

The PLLA/10mSiNP was adopted for Mg stent degradation test due to its coating stability and significantly improved corrosion resistance. This

stent degradation test is distinct from the previous corrosion test on Mg plate specimens, since mechanical deformation was applied on the coating layer during stent expansion. According to **Figure 3.5Fb**, where the remaining volume (%) was calculated against an initial total volume of stent, the composite coating protected Mg stent far more effectively than the pure one. For the pure PLLA-coated stent, its volume decreased continuously, and after 3 days of immersion, several struts and bridge parts between them were broken and separated, with the result that 54.27 % was lost for 12 days. The PLLA/10mSiNP-coated Mg stent, on the other hand, remained 72.84 % of its initial morphology at the last day, revealing significantly mild degradation rate (**Figure 3.5Fa**).

3.3.4. *In vitro* endothelial cell assays

To assess the endothelial cell responses to the Mg samples with pure PLLA and PLLA/mSiNP nanocomposite coatings, we investigated the HUVEC adhesion morphology, surface coverage area, and proliferation (**Figure 3.7**). **Figure 3.7A** shows representative CLSM images of the endothelial cells adhering to each coating surface after 1 d of culture. A considerably small number of cells adhered and barely spread on the surface of the pure PLLA coating, retaining near-spherical cell morphology with few cellular protrusions (**Figure 3.7Aa**). In contrast, on the PLLA/mSiNP nanocomposite coatings, the

number of adhered cells appears to increase progressively on the surfaces with increasing the amount of mSiNP, and noticeably, the HUVECs adhere more and spread well on the surfaces of PLLA/10mSiNP and PLLA/20mSiNP coatings, exhibiting polygonal adhering morphologies with distinct filopodia and lamellipodia structures (**Figure 3.7Ab–d**). From the quantitative measurement (**Figure 3.7B**), pure PLLA coating showed the lowest level of cell coverage area of $10.5 \pm 1.70\%$, while the PLLA/mSiNP nanocomposite coatings exhibited significantly higher levels of cell coverage areas than the pure PLLA, showing $26.0 \pm 3.02\%$, $31.4 \pm 6.14\%$, and $46.4 \pm 12.3\%$ for PLLA/5mSiNP, PLLA/10mSiNP, and PLLA/20mSiNP, respectively. HUVEC proliferation was also greatly affected when mSiNP was incorporated into the PLLA coating matrix. After 3 days of culturing, the HUVEC proliferation levels on the PLLA/mSiNP nanocomposite coatings were higher than those on the pure PLLA and also demonstrated an increasing tendency with mSiNP amounts (**Figure 3.7C**). In particular, on the PLLA/10mSiNP and PLLA/20mSiNP nanocomposite coatings, the cell proliferation levels were approximately three and four times higher than that of the pure PLLA coating with statistical significance ($P < 0.05$).

The rates of HUVEC migration distance on each coating surface were examined after removing the barrier and observing the cell inhibition zone at the predetermined time (3 and 24 h) (**Figure 3.8A**). As shown in **Figure**

3.8B&C, all samples showed gradual migration of HUVECs into the cell inhibition zone, and the gap between the cell layers decreased with culturing time. However, in terms of the relative migration distance, a significant difference was found between the pure PLLA and PLLA/mSiNP nanocomposite coatings. In particular, on PLLA/10mSiNP and PLLA/20mSiNP coatings, HUVECs rapidly migrated, showing approximately 30% of the migration area after 3 h of cell culturing, and an 80% cell migration area was reached only after 24 h, whereas the HUVEC migration area on the pure PLLA was only 5% and 45% after 3 and 24 h of incubation, respectively. The cells on the PLLA/5mSiNP coating also exhibited a higher rate of cell migration compared to the pure PLLA coating, but the difference was not very significant compared to the PLLA/10mSiNP and PLLA/20mSiNP coatings.

3.4. Discussion

Although Mg and its alloys are promising candidates for the fabrication of biodegradable vascular stents, their excessively high degradation rate is a fundamental challenge for their practical use in medical applications [83]. To overcome this limitation, four typical strategies have been suggested, which involves purification to remove impurities in the Mg matrix that can cause galvanic corrosion, alloying treatment for enhancing not only corrosion resistance but structural integrity, metal matrix composite by protecting corroded parts or formulating surface mineralization, and bioceramic or biopolymer coating to regulate degradation rate [112]. Among the numerous techniques for coating or surface modification of Mg implants, polymeric coating is widely applied because it can endure structural deformation during a balloon-assisted expansion procedure [83, 98, 113]. However, to the best of our knowledge, few studies have investigated a feasible coating system for Mg stents that can not only suppress degradation but also promote biocompatibility while minimizing the required total coating thickness to less than 5 μm . As the thick polymeric coating may not endure stable coating deformations during the stent deployment process, it is practically important to provide sufficient degradation resistance to the Mg stent, even with a thin coating thickness [99]. In this study, we developed a bifunctional PLLA/mSiNP nanocomposite coating that facilitated robust corrosion resistance and remarkably promoted

endothelialization by incorporating silica nanoparticles into PLLA, while maintaining a coating thickness of less than 4 μm (**Table 3.1** and **Figure 3.9**).

The necessity for surface modification of the silica nanoparticles should be considered prior to evaluating the physiological and biological properties of the PLLA/mSiNP nanocomposite coatings because the phase separation between the hydrophobic polymer matrix and hydrophilic ceramic nanoparticles commonly occurs via strong hydrophobic–hydrophilic repulsion forces between them [114, 115]. Therefore, alkyl-functionalized mSiNPs, treated with HDTMS with long carbon chains, were utilized instead of hydrophilic SiNPs obtained via the Stöber method to allow nanoparticles to disperse uniformly in the hydrophobic PLLA matrix and exploit its good water penetration resistance [111]. As shown in **Figure 3.2A&B**, although the morphology and size of the particles before and after the surface treatment barely changed, the characteristic peaks for C-H bending at 2923 and 2850 cm^{-1} were observed only for mSiNPs on FT-IR analysis, indicating that its surface was alkylated by HDTMS. Additionally, from the XPS analysis, the mSiNP clearly showed C 1s region originated from HDTMS, while only tiny one appeared on SiNP due to inevitable surface contamination (**Figure 3.10Aa&Bb**). The peaks at 284.4 eV, 285.0 eV, and 286.2 eV associate to the C-C, $\text{CH}_3\text{-Si}$, and C-O from the C 1s spectrum of mSiNP, respectively. For Si 2p spectrum, the SiNP revealed two peaks at 103.2 eV and 103.9 eV

corresponding to O-Si-O and Si-OH (**Figure 3.10Aa'**), however, an additional peak for Si-C was observed at 102.5 eV on mSiNP (**Figure 3.10Bb'**), the integrated intensity of which was 17 %. Therefore, both analysis, FT-IR and XPS, verified the surface of mSiNP was successfully modified into hydrophobic. The surface wetting angle was measured after each particle was dispersed in ethanol by sonication and overnight agitation to coat a slide glass. The alkylation process significantly increased the WCA up to 103°, ensuring that the surface of the mSiNP was successfully modified into hydrophobic properties (**Figure 3.2C**). The enhanced dispersion of mSiNP in PLLA is shown in **Figure 3.11A**. The mSiNP dispersed far more uniformly into a PLLA matrix without forming large agglomerated clusters compared to the bare one. This uniform dispersion contributed to not only the relatively even surface morphology but also the mechanical strength, with a higher tensile extension (11.5%), while the fracture on the PLLA/SiNP film occurred at only 3.5% of deformation, as the agglomerated site caused stress concentration (**Figure 3.11B&C**) [116]. Furthermore, the corrosion resistance of PLLA/mSiNP was superior to it of PLLA/SiNP with the same concentration of the embedded particles, and also the standard deviation among the specimens was smaller than PLLA/SiNP, exhibiting relatively uniform property (**Figure 3.11D**). Thus, both hydrophobic surface and homogeneous dispersion of mSiNP protected the substrate against corrosive medium by resisting the water penetration through the surface and elongating the water transportation through the matrix

effectively [117, 118]

The PLLA/mSiNP nanocomposite coating on the Mg substrate was prepared with different amounts of mSiNP (up to 20 wt%), and their surface morphology, chemical composition, wettability, and surface roughness were compared with those of the pure PLLA coating. On the surface of the PLLA/mSiNP coatings, the incorporated mSiNPs were partially exposed on the outermost surface of the coating layer, but they still maintained a defectless coating structures (**Figure 3.1A**), and the presence of mSiNPs on the surface was also chemically identified via FT-IR analysis (**Figure 3.1B**). However, the PLLA/20mSiNP nanocomposite coating exhibited many aggregated mSiNPs on the surface at the sub-micron scale and the highest surface roughness (R_q) among all coated samples (**Figure 3.1Ad** and **Figure 3.3**). Although ceramic nanoparticles could play a role in reinforcing the polymer matrix, many parameters directly affect the mechanical properties of the nanocomposite, such as reinforcement size, surface functionalization, interfacial adhesion, and dispersion state [119]. In PLLA/mSiNP nanocomposite coating system, the imbedded silica nanoparticles didn't affect coating adhesion strength, exhibiting the critical load around 41 mN in all the coatings (**Figure 3.12**) when micro-scratch test was performed using a micro-scratch tester with a total length of 500 μm , normal force range of 10-300 mN, scratch speed of 3 $\mu\text{m/s}$, and indenter radius of 12.5 μm , but mechanical strength. In particular, because

structural entanglement between the polymer matrix and ceramic nanoparticles is regarded as the main reason for mechanical strengthening under deformation conditions [119, 120], overloaded mSiNPs (20 wt%) with poor dispersion stability in the PLLA matrix should minimize the magnitude of the interaction between the mSiNP and PLLA and adversely affect the mechanical behavior of the nanocomposite, resulting in a decrease in the elastic modulus and UTS, compared to the PLLA/10mSiNP (**Figure 3.4A&B**) [70, 121]. In addition, the aggregated mSiNPs on the surface could induce the formation of cracks under tensile and flexural loading via inhomogeneous and localized stress distribution, which in turn deteriorates the coating stability during the stent deployment process (**Figure 3.4Cd'**) [122]. It is common that the critical concentration of the nanofillers exists to reinforce the host matrix, regardless of material type such as alloy or polymer/ceramic composite, since the cohesion between the aggregated particles leads to deterioration of mechanical strength; that is, PLLA/10mSiNP was regarded as a critical condition for reinforcements in this composite coating system [123, 124].

In terms of biocompatibility, it is important that the PLLA/mSiNP nanocomposite coating should provide a stable biological environment for rapid re-endothelialization over the coated Mg stent. Therefore, enhanced corrosion resistance could restrict a local alkaline environment and overdose of releasing Mg ions, which provide benefits for cell adhesion and proliferation

[113, 125]. The accumulation rate of the evolved hydrogen gas resulting from corrosion also affected the stable environment for cell growth on the coating, since the formation of excessive hydrogen gas pockets may cause vacancies between the coating and the Mg substrate, or eventually separation of the protective layer and then exposure of a large region of the substrate [126]. As shown in **Figure 3.5**, the introduction of the mSiNPs hindered the degradation of the Mg substrate, leading to a small amount of evolved hydrogen gas and a low concentration of the released Mg ions. More importantly, there was no H₂ gas evolution until 7 days of immersion with the PLLA/10mSiNP and PLLA/20mSiNP nanocomposite coatings, while it was rapidly corroded with the pure PLLA coating, causing a noticeable localized coating failure because of the enormous H₂ gas pockets. The pH value was also evaluated by immersing the bare (un-coated), PLLA-coated, and PLLA/mSiNP-coated Mg substrates in 40mL of SBF solution at 37 °C (**Figure 3.6C**). The initial pH value of SBF was 7.3. The pH of bare Mg increased immediately and reached 10.15 after 12 days of immersion due to rapid corrosion, while the PLLA and PLLA/mSiNP-coated Mg exhibited slight pH decrease in the initial stage owing to degradation of the PLLA, followed by gradual increase. The alkaline shift was more moderate with the PLLA coating, implying the hydrolysis of PLLA may neutralize and mitigate the pH change, and also decreased with increasing amount of mSiNP [118, 127]. This result has a good agreement with the previous corrosion test (**Figure 3.5**), which indicates PLLA/mSiNP nanocomposite exhibited excellent

corrosion resistance with slower pH increase. In addition, when the coated Mg stent with PLLA and PLLA/10mSiNP were inserted and deployed into the silicone tube under the SBF immersion condition, the PLLA/10mSiNP coating practically offer excellent corrosion resistance to the Mg stent, showing higher amount of remained original stent shapes and volumes than that of pure PLLA coating during the entire immersion period. Typically, hydrophobic surface layers not only provide a less accessible surface to the corrosive medium but also lead to retarding its penetration to the Mg substrate, thus delaying the initial stage of corrosive attach and slowing the overall kinetic corrosion processes [118, 128, 129]. In this study, the exposed mSiNPs contributed to the hydrophobicity of the coating, which could disturb the initial water penetration, and the embedded particles can also elongate the water transport path to prolong the time delay until contact with the Mg substrate [104, 105, 130].

Along with the corrosion resistance, there are many factors influencing the cellular behavior and vascular regeneration around the implanted materials, such as surface wettability, topography, chemical composition, and ionic concentration of the surroundings [131, 132]. As shown in **Figure 3.7** and **Figure 3.8**, the endothelial cell functions, including early attachment, migration, and proliferation, tended to be gradually enhanced with increasing mSiNP amount. In general, Si is dissolved into silicic acid (Si(OH)_4) in an aqueous environment, and its dissolution behavior depends on several

parameters such as the size, porosity, surface functional group, and pH or temperature of the media. The Si ions released from $\text{Si}(\text{OH})_4$ are known to be a driving factor of angiogenesis by activating the synthesis of vascular endothelial growth factor (VEGF) and its receptor (VEGF receptor 2), resulting in increased proliferation, migration motility, and differentiation of endothelial cells [32]. The extent of hydrophobic modification of silica influences degradation [133], so the reaction time with HDTMS in this study was set to 15 min. The modified silica nanoparticles embedded in the nanocomposite coating on Mg sustained the release of Si without any sign of saturation for 8 days. In addition, it has been reported that the roughened surface morphology can encourage HUVEC adhesion on the surface and secrete several intracellular cytokines that can further promote the tight adhesion of cells via formation of filopodia- and lamellipodia-like cell protrusion [134, 135]. Thus, it can be concluded that the synergistic effect of the Si-rich environment and roughened surface of PLLA/mSiNP should improve endothelial cell activity, including initial attachment, migration, and proliferation, implying rapid endothelialization over the Mg stents.

3.5. Conclusion

In this study, we developed a bifunctional PLLA/mSiNP nanocomposite coating on a Mg stent to enhance the corrosion resistance and endothelial cellular affinity. Hydrophobic surface modification of the silica nanoparticles enabled uniform dispersion in the PLLA matrix, and the PLLA/mSiNP nanocomposites exhibited excellent mechanical properties without any noticeable coating delamination or Mg substrate exposure during stent deployment process. Incorporation of the mSiNP into the PLLA coating significantly protected Mg substrate from rapid degradation by disturbing the penetration of corrosion media through the nanocomposite coating. The roughened surface and Si-rich environment of the PLLA/mSiNP nanocomposite coatings triggered the initial adhesion, migration, and proliferation of endothelial cells. These results suggest that the PLLA/mSiNP nanocomposite coatings can provide a practical and reliable strategy to improve corrosion resistance and clinical outcomes of biodegradable Mg-based vascular stents.

Sample	Average coating thickness (μm)
PLLA	3.12 ± 0.071
PLLA/5mSiNP	3.77 ± 0.102
PLLA/10mSiNP	3.73 ± 0.036
PLLA/20mSiNP	3.96 ± 0.118

Table 3.1. Average thickness of pure PLLA and PLLA/mSiNP nanocomposite coatings.

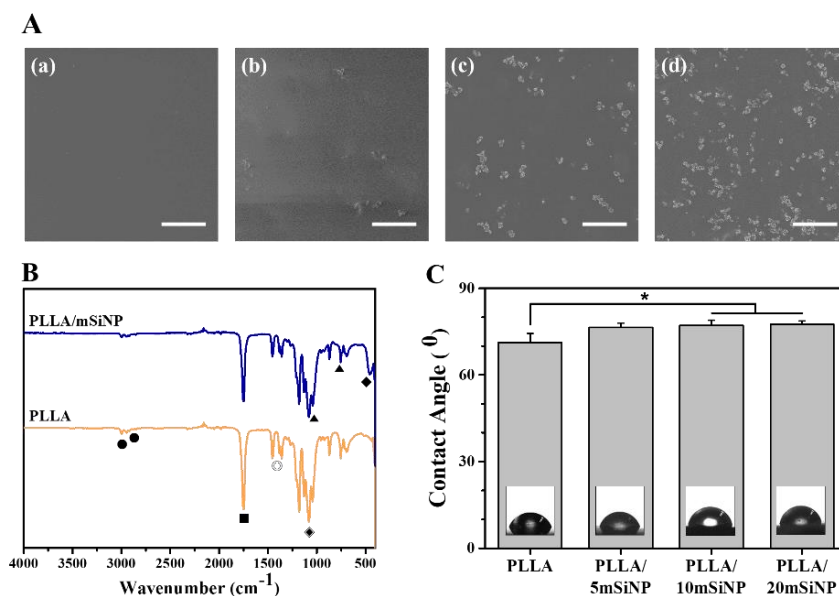


Figure 3.1. (A) Surface morphology of (a) pure PLLA, (b) PLLA/5mSiNP, (c) PLLA/10mSiNP, and (d) PLLA/20mSiNP coating layer on Mg alloy (scale bar = 10 μm). (B) FT-IR spectra of pure PLLA and PLLA/mSiNP nanocomposite (●: C-H stretching, ■: C=O stretching, ⊙: C-H bending, ◆: C-O stretching, ▲: Si-O-Si stretching, ◇: Si-O-Si bending). (C) Water contact angle measurement on (a) ~ (d). (* $p < 0.05$)

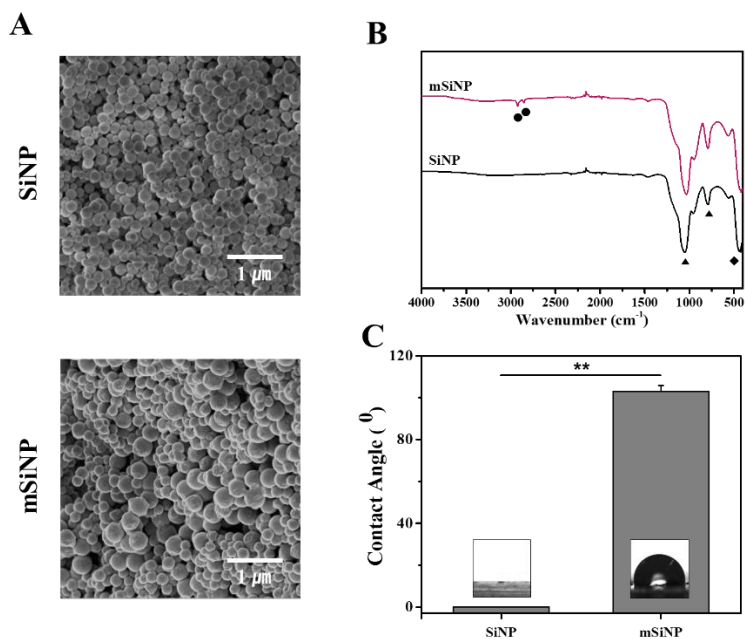


Figure 3.2. (A) SEM images of silica nanoparticles (SiNP) and surface-modified hydrophobic silica nanoparticles (mSiNP). (B) FT-IR spectra of SiNP and mSiNP (●: C-H stretching, ▲: Si-O-Si stretching, ◆: Si-O-Si bending). (C) Water contact angle (WCA) measurement on a slide glass coated with the SiNP and mSiNP (** $p < 0.005$).

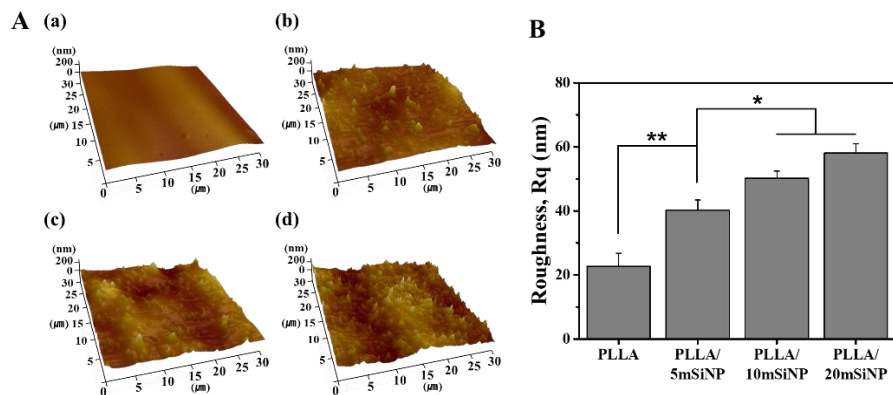


Figure 3.3. (A) AFM surface topography of (a) pure PLLA, (b) PLLA/5mSiNP, (c) PLLA/10mSiNP, and (d) PLLA/20mSiNP coating layer on Mg alloy and (B) their measured root mean square roughness (Rq) (* $p < 0.05$ and ** $p < 0.005$).

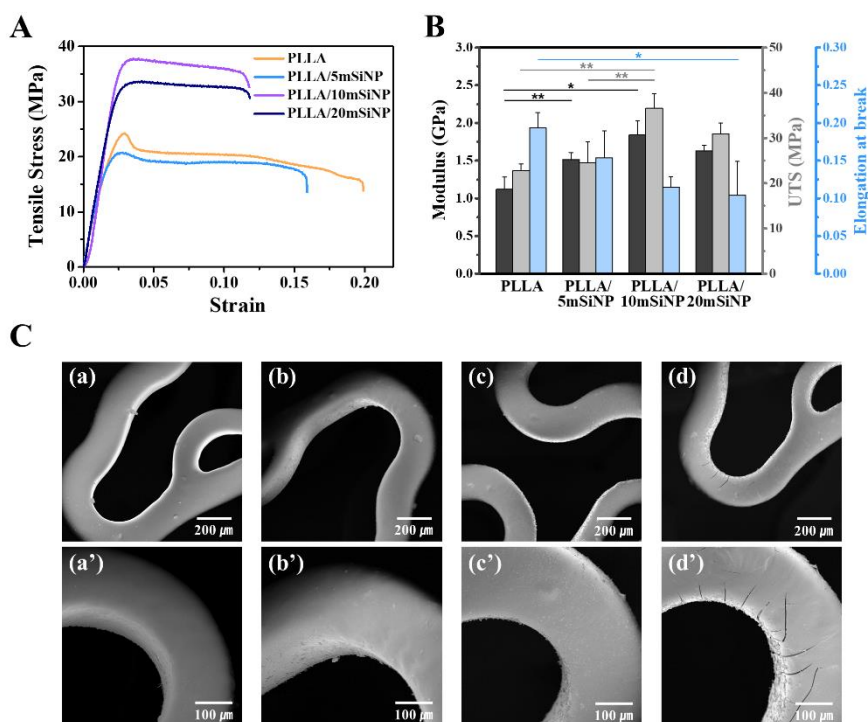


Figure 3.4. (A) The representative stress–strain curve and (B) summary of mechanical properties of pure PLLA and PLLA/mSiNP nanocomposite films fabricated by solvent-casting method (* $p < 0.05$ and ** $p < 0.005$). (C) Surface morphology of WE43 stent coated with (a) pure PLLA, (b) PLLA/5mSiNP, (c) PLLA/10mSiNP, and (d) PLLA/20mSiNP after the stent expansion process, and their magnified images at the curved part (a') ~ (d') in order.

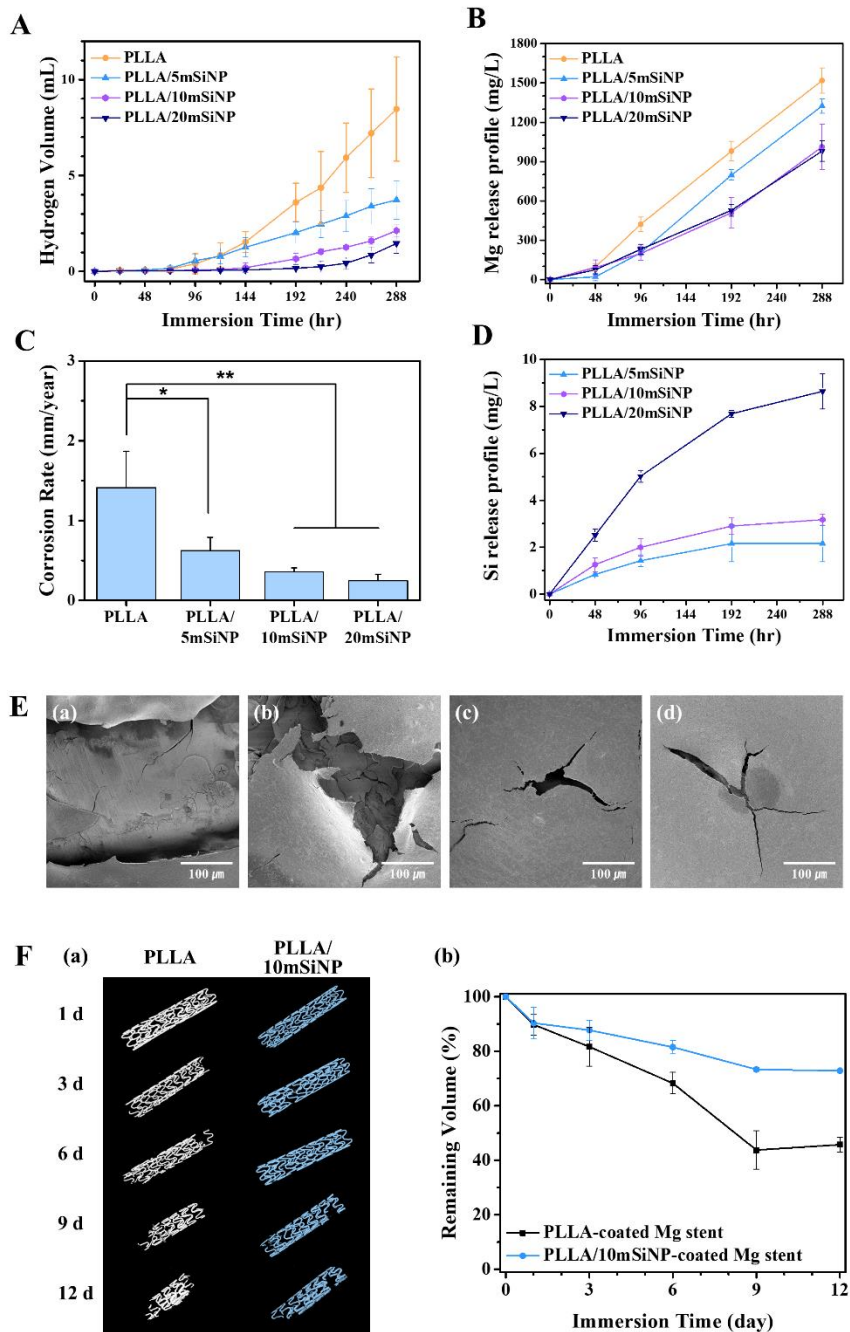


Figure 3.5. (A) Evolved H₂ gas volume and (B) released Mg ion after immersing Mg alloys coating with pure PLLA, PLLA/5mSiNP, PLLA/10mSiNP, and PLLA/20mSiNP in SBF. (C) Theoretical corrosion rate based on the amount of hydrogen volume (*p < 0.05 and **p < 0.005). (D) Si ion release profile tracking after immersing each specimen in SBF solution for 12 days. (E) Surface morphology of (a) pure PLLA, (b) PLLA/5mSiNP, (c) PLLA/10mSiNP, and (d) PLLA/20mSiNP coating layer after 12 days. (F) (a) The representative μ -CT images of pure PLLA-coated and PLLA/10mSiNP-coated Mg stent and (b) their remaining volume change during corrosion test.

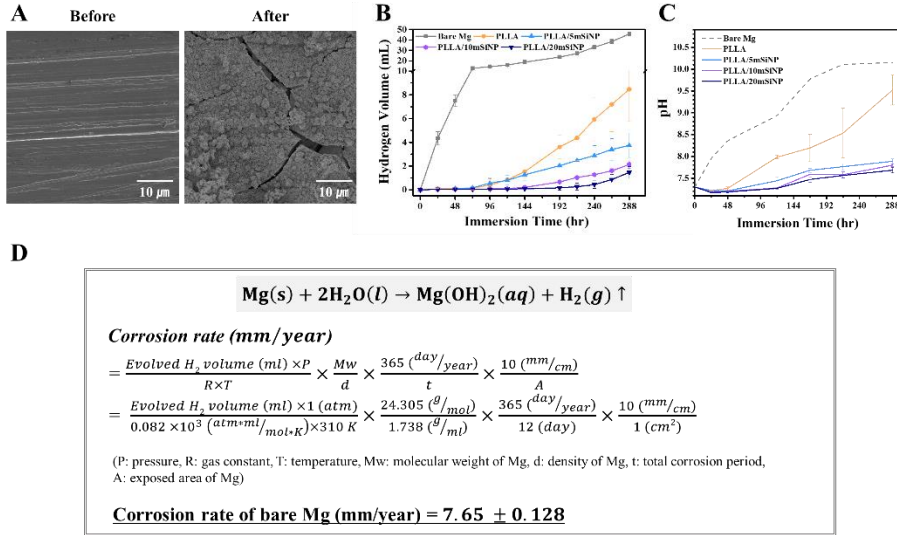


Figure 3.6. (A) SEM images of bare Mg plate before and after corrosion test for 12 days. (B) Evolved hydrogen gas volume of bare Mg (non-coated). (C) The pH value of the solution after immersing the bare, PLLA-coated, and PLLA/mSiNP-coated Mg specimens in 40 mL of SBF. (D) The calculation process of theoretical corrosion rate under ideal condition and the resulted value in the case of bare Mg.

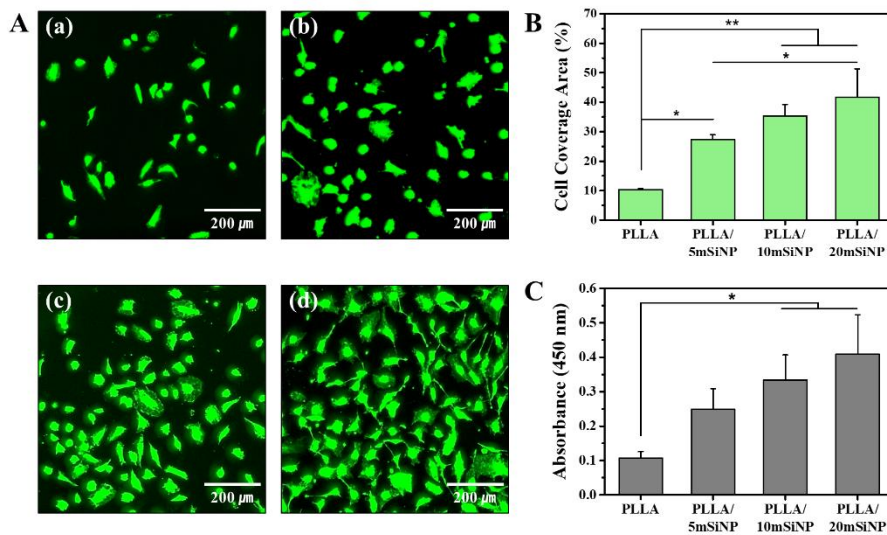


Figure 3.7. (A) CLSM images of adhered endothelial cells and (B) their coverage area on (a) pure PLLA, (b) PLLA/5mSiNP, (c) PLLA/10mSiNP, and (d) PLLA/20mSiNP coating layer on Mg alloy substrate after 1 day of culturing. (C) Cell proliferation on each specimen after culturing for 3 days (* $p < 0.05$ and ** $p < 0.005$).

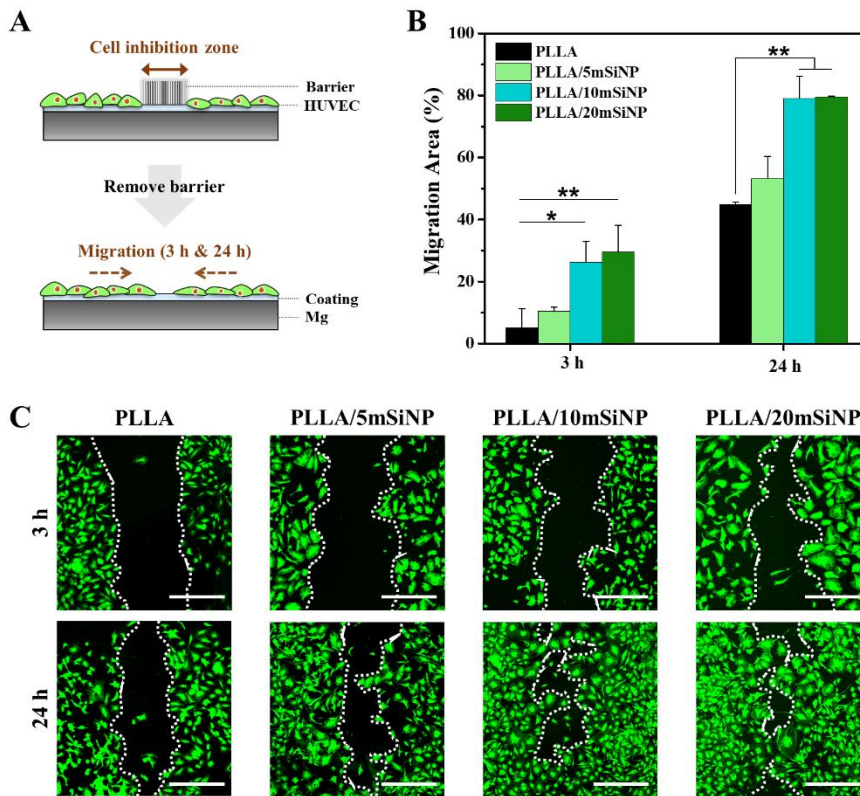


Figure 3.8. (A) Schematic illustration of cell migration test. (B) Cell migration area was calculated over the area of initial cell inhibition zone. (C) CLSM images of endothelial cells on each specimen at 3 and 24 h after removing the barrier (scale bar = 500 μ m).

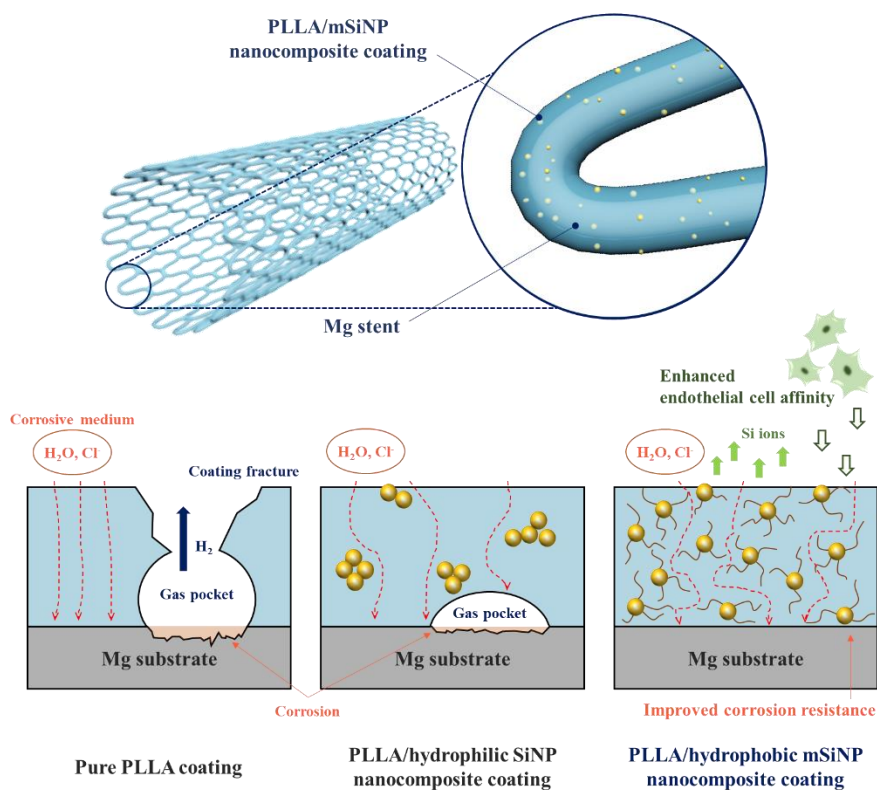


Figure 3.9. Schematic illustration of bifunctional PLLA/mSiNP nanocomposite coating on the Mg stent surface.

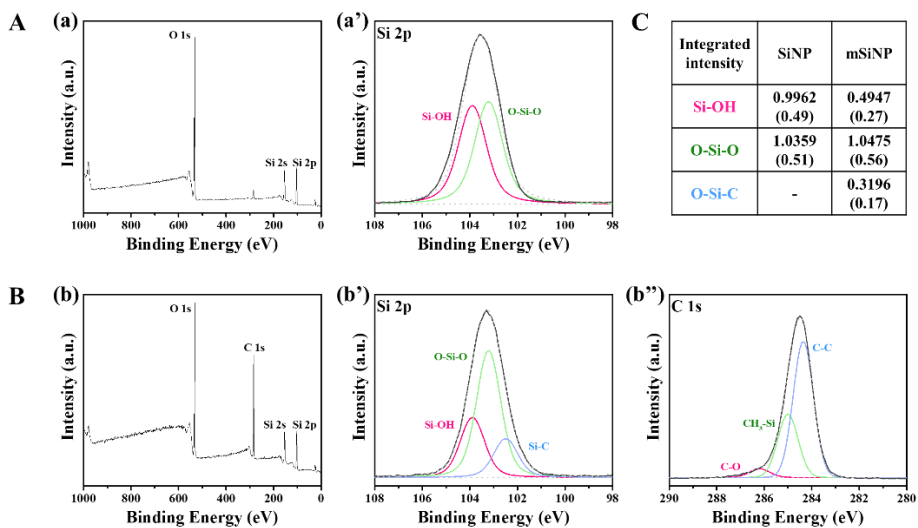


Figure 3.10. (A) (a) XPS full spectra and (b) high resolution spectra of Si 2p for SiNP. (B) (b) XPS full spectra and high resolution spectra of (b') Si 2p and (b'') C 1s for mSiNP. (C) Integrated intensity of each Si 2p peak for SiNP and mSiNP and the relative value was calculated in a bracket.

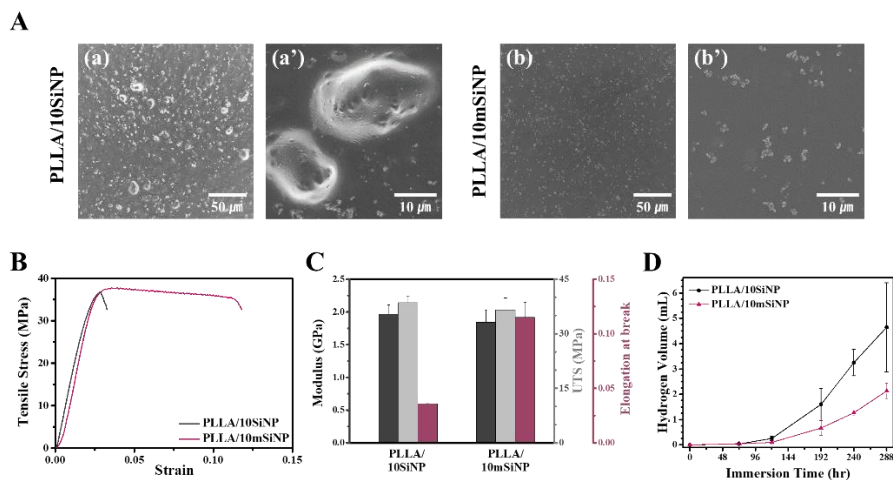


Figure 3.11. (A) SEM images of the PLLA composite coating containing 10 wt % of (a) bare silica nanoparticles (Si) and (b) surface-modified silica nanoparticles (mSi). (a') and (b') refer a magnified image for (a) and (b), respectively. (B) Tensile stress-strain curve of the PLLA/10Si and PLLS/10mSi film fabricated via solvent-casting method, and (C) their modulus, UTS, and elongation at break. (D) Evolved hydrogen gas volume after immersing PLLA/10SiNP and PLLA/10mSiNP for 12 days.

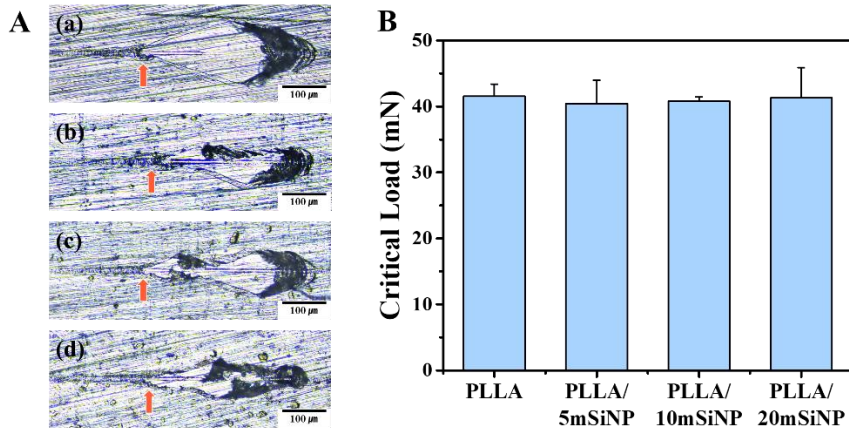


Figure 3.12. Micro-scratch test on the PLLA and PLLA/mSiNP coatings.
(A) Optic images of scratch track on (a) pure PLLA, (b) PLLA/5mSiNP, (c) PLLA/10mSiNP, and (d) PLLA/20mSiNP coating layer and **(B)** their critical load. (The orange arrows indicate the delamination point)

Chapter 4.

Conclusion

This thesis aimed to improve both biological and physical functions of biodegradable vascular implants by incorporating silica into polymer matrix, emphasizing the merits of each material. As polymeric materials exhibit similar mechanical properties to the native ECM and silica promotes angiogenesis, the polymer/silica composite mutually complemented each other to possess the required characteristics.

In the first study, a PCL-based bilayer vascular graft was successfully fabricated via electrospinning. To fabricate randomly-distributed PCL/silica nanofibrous membrane for the outer layer, silica xerogel was in-situ synthesized in the polymer matrix to form a mesoporous nanoskeleton structure uniformly over the polymer fibers. The PCL/silica composite not only displayed more than twice as high mechanical properties as the pure PCL but enhanced cellular affinity of fibroblast cells. Additionally, a relatively thin inner layer of PCL/collagen composite was aligned parallel to blood flow for rapid endothelialization of the luminal surface. Thus, the exquisite artificial grafts accomplished great biocompatibility with both endothelial and fibroblast cells, resisting physical distortion from blood pressure.

In the second study, the surface-modified silica nanoparticles were incorporated into PLLA coating for biodegradable Mg stents in order to improve bioactivity of endothelial cells and corrosion resistance. To disperse the silica nanoparticle in the PLLA homogeneously and enhance surface

hydrophobicity of the nanofiller, the silica nanoparticles were functionalized with HDTMS under base-catalyzed condition, and then introduced to disturb penetration of corrosive media through PLLA/mSiNP coating. The relatively slow H₂ gas evolution and Mg ion release profile demonstrated the enhanced anti-corrosion property, also identified by applying on stent prototype. The nanocomposite coating also encouraged biological activity of endothelial cells due to its roughened surface and Si-rich environment. A novel PLLA/mSiNP nanocomposite coating, hence, promoted rapid vascular tissue regeneration as well as prevented the explosive degradation of Mg stents.

In conclusion, we varied the materials and design of polymer/silica composite that offers great biocompatibility and physical functions including mechanical strength, stability, and corrosion resistance. The incorporated silica was transformed into the adequate morphology and functional moiety for specific application area where the vascular implants are to be inserted. A sole material has difficult performing various properties that seldom coexist, so such composite materials have attracted much attention.

References

- [1] S.S. Virani, A. Alonso, H.J. Aparicio, E.J. Benjamin, M.S. Bittencourt, C.W. Callaway, A.P. Carson, A.M. Chamberlain, S. Cheng, F.N. Delling, M.S.V. Elkind, K.R. Evenson, J.F. Ferguson, D.K. Gupta, S.S. Khan, B.M. Kissela, K.L. Knutson, C.D. Lee, T.T. Lewis, J. Liu, M.S. Loop, P.L. Lutsey, J. Ma, J. Mackey, S.S. Martin, D.B. Matchar, M.E. Mussolino, S.D. Navaneethan, A.M. Perak, G.A. Roth, Z. Samad, G.M. Satou, E.B. Schroeder, S.H. Shah, C.M. Shay, A. Stokes, L.B. VanWagner, N.-Y. Wang, C.W. Tsao, Heart Disease and Stroke Statistics-2021 Update, *Circulation* 143(8) (2021) e254-e743.
- [2] J. Li, K. Zhang, N. Huang, Engineering Cardiovascular Implant Surfaces to Create a Vascular Endothelial Growth Microenvironment, *Biotechnology Journal* 12(12) (2017) 1600401.
- [3] E. Ercolani, C. Del Gaudio, A. Bianco, Vascular tissue engineering of small-diameter blood vessels: reviewing the electrospinning approach, *Journal of Tissue Engineering and Regenerative Medicine* 9(8) (2015) 861-888.
- [4] C.H. Riedel, M. Tietke, K. Alfke, R. Stingele, O. Jansen, Subacute Stent Thrombosis in Intracranial Stenting, *Stroke* 40(4) (2009) 1310-1314.
- [5] P.M. Looser, L.K. Kim, D.N. Feldman, In-Stent Restenosis: Pathophysiology and Treatment, *Current Treatment Options in Cardiovascular Medicine* 18(2) (2016) 10.
- [6] P. Mallis, A. Kostakis, C. Stavropoulos-Giokas, E. Michalopoulos, Future Perspectives in Small-Diameter Vascular Graft Engineering, *Bioengineering*

7(4) (2020) 160.

[7] A. Hasan, A. Memic, N. Annabi, M. Hossain, A. Paul, M.R. Dokmeci, F. Dehghani, A. Khademhosseini, Electrospun scaffolds for tissue engineering of vascular grafts, *Acta Biomaterialia* 10(1) (2014) 11-25.

[8] S. Ravi, E.L. Chaikof, Biomaterials for vascular tissue engineering, *Regen Med* 5(1) (2010) 107-120.

[9] J.J.D. Henry, J. Yu, A. Wang, R. Lee, J. Fang, S. Li, Engineering the mechanical and biological properties of nanofibrous vascular grafts for in situ vascular tissue engineering, *Biofabrication* 9(3) (2017) 035007.

[10] S.K. Norouzi, A. Shamloo, Bilayered heparinized vascular graft fabricated by combining electrospinning and freeze drying methods, *Materials Science and Engineering: C* 94 (2019) 1067-1076.

[11] J.P. Cuenca, A. Padalhin, B.-T. Lee, Small-diameter decellularized vascular graft with electrospun polycaprolactone, *Materials Letters* 284 (2021) 128973.

[12] L.-D. Hou, Z. Li, Y. Pan, M. Sabir, Y.-F. Zheng, L. Li, A review on biodegradable materials for cardiovascular stent application, *Frontiers of Materials Science* 10(3) (2016) 238-259.

[13] S. Buccheri, D. Capodanno, Bioabsorbable stents: only bad news?, *European Heart Journal Supplements* 21(Supplement_B) (2019) B28-B30.

- [14] S. Ramcharitar, P.W. Serruys, Fully Biodegradable Coronary Stents, *American Journal of Cardiovascular Drugs* 8(5) (2008) 305-314.
- [15] M. Echeverry-Rendon, J.P. Allain, S.M. Robledo, F. Echeverria, M.C. Harmsen, Coatings for biodegradable magnesium-based supports for therapy of vascular disease: A general view, *Materials Science and Engineering: C* 102 (2019) 150-163.
- [16] Y. Zhu, K. Yang, R. Cheng, Y. Xiang, T. Yuan, Y. Cheng, B. Sarmento, W. Cui, The current status of biodegradable stent to treat benign luminal disease, *Materials Today* 20(9) (2017) 516-529.
- [17] K.-H. Cheon, C. Gao, M.-H. Kang, H.-D. Jung, T.-S. Jang, H.-E. Kim, Y. Li, J. Song, A crack-free anti-corrosive coating strategy for magnesium implants under deformation, *Corrosion Science* 132 (2018) 116-124.
- [18] S. Abdulghani, G.R. Mitchell, Biomaterials for In Situ Tissue Regeneration: A Review, *Biomolecules* 9(11) (2019) 750.
- [19] J. Wang, L. Wang, Z. Zhou, H. Lai, P. Xu, L. Liao, J. Wei, Biodegradable Polymer Membranes Applied in Guided Bone/Tissue Regeneration: A Review, *Polymers* 8(4) (2016) 115.
- [20] S. Yan, Y. Li, Y.-C. Jiang, Y. Xu, D. Wang, X. Zhang, Q. Li, L.-S. Turng, Expanded polytetrafluoroethylene/silk fibroin/salicin vascular graft fabrication for improved endothelialization and anticoagulation, *Applied Surface Science* 542 (2021) 148610.

- [21] L. Yu, E.R. Newton, D.C. Gillis, K. Sun, B.C. Cooley, A.N. Keith, S.S. Sheiko, N.D. Tsihlis, M.R. Kibbe, Coating small-diameter ePTFE vascular grafts with tunable poly(diols-co-citrate-co-ascorbate) elastomers to reduce neointimal hyperplasia, *Biomaterials Science* (2021).
- [22] M. Dziadek, E. Stodolak-Zych, K. Cholewa-Kowalska, Biodegradable ceramic-polymer composites for biomedical applications: A review, *Materials Science and Engineering: C* 71 (2017) 1175-1191.
- [23] S.-Y. Fu, X.-Q. Feng, B. Lauke, Y.-W. Mai, Effects of particle size, particle/matrix interface adhesion and particle loading on mechanical properties of particulate–polymer composites, *Composites Part B: Engineering* 39(6) (2008) 933-961.
- [24] H. Zou, S. Wu, J. Shen, Polymer/Silica Nanocomposites: Preparation, Characterization, Properties, and Applications, *Chemical Reviews* 108(9) (2008) 3893-3957.
- [25] U. Schubert, *Chemistry and Fundamentals of the Sol–Gel Process*, The Sol-Gel Handbook 2015, pp. 1-28.
- [26] D. Arcos, M. Vallet-Regí, Sol–gel silica-based biomaterials and bone tissue regeneration, *Acta Biomaterialia* 6(8) (2010) 2874-2888.
- [27] I.A. Rahman, V. Padavettan, Synthesis of Silica Nanoparticles by Sol-Gel: Size-Dependent Properties, Surface Modification, and Applications in Silica-Polymer Nanocomposites—A Review, *Journal of Nanomaterials* 2012 (2012) 132424.

- [28] A. Mehner, J. Dong, T. Prenzel, W. Datchary, D.A. Lucca, Mechanical and chemical properties of thick hybrid sol–gel silica coatings from acid and base catalyzed sols, *Journal of Sol-Gel Science and Technology* 54(3) (2010) 355-362.
- [29] J.G. Croissant, Y. Faticiev, A. Almalik, N.M. Khashab, Mesoporous Silica and Organosilica Nanoparticles: Physical Chemistry, Biosafety, Delivery Strategies, and Biomedical Applications, *Advanced Healthcare Materials* 7(4) (2018) 1700831.
- [30] S.P. Hadipour Moghaddam, R. Mohammadpour, H. Ghandehari, In vitro and in vivo evaluation of degradation, toxicity, biodistribution, and clearance of silica nanoparticles as a function of size, porosity, density, and composition, *Journal of Controlled Release* 311-312 (2019) 1-15.
- [31] J.G. Croissant, C.J. Brinker, Chapter Eight - Biodegradable Silica-Based Nanoparticles: Dissolution Kinetics and Selective Bond Cleavage, in: F. Tamanoi (Ed.), *The Enzymes*, Academic Press 2018, pp. 181-214.
- [32] K. Dashnyam, A. El-Fiqi, J.O. Buitrago, R.A. Perez, J.C. Knowles, H.W. Kim, A mini review focused on the proangiogenic role of silicate ions released from silicon-containing biomaterials, *J Tissue Eng* 8 (2017) 2041731417707339.
- [33] G.H. Fong, K. Takeda, Role and regulation of prolyl hydroxylase domain proteins, *Cell Death & Differentiation* 15(4) (2008) 635-641.
- [34] H.Y. Ang, Y.Y. Huang, S.T. Lim, P. Wong, M. Joner, N. Foin, Mechanical behavior of polymer-based vs . metallic-based bioresorbable stents, *Journal of*

Thoracic Disease (2017) S923-S934.

[35] D.N. Ghista, F. Kabinejadian, Coronary artery bypass grafting hemodynamics and anastomosis design: a biomedical engineering review, *BioMedical Engineering OnLine* 12(1) (2013) 129.

[36] M. Iijima, H. Aubin, M. Steinbrink, F. Schiffer, A. Assmann, R.D. Weisel, Y. Matsui, R.-K. Li, A. Lichtenberg, P. Akhyari, Bioactive coating of decellularized vascular grafts with a temperature-sensitive VEGF-conjugated hydrogel accelerates autologous endothelialization in vivo, *Journal of Tissue Engineering and Regenerative Medicine* 12(1) (2018) e513-e522.

[37] A. Guildford, M. Santin, G.J. Phillips, 7 - Cardiovascular stents, in: T. Gourlay, R.A. Black (Eds.), *Biomaterials and Devices for the Circulatory System*, Woodhead Publishing 2010, pp. 173-216.

[38] T. Koppara, Q. Cheng, K. Yahagi, H. Mori, O.D. Sanchez, J. Feygin, E. Wittchow, F.D. Kolodgie, R. Virmani, M. Joner, Thrombogenicity and Early Vascular Healing Response in Metallic Biodegradable Polymer-Based and Fully Bioabsorbable Drug-Eluting Stents, *Circulation: Cardiovascular Interventions* 8(6) (2015) e002427.

[39] N.K. Awad, H. Niu, U. Ali, Y.S. Morsi, T. Lin, Electrospun Fibrous Scaffolds for Small-Diameter Blood Vessels: A Review, *Membranes* 8(1) (2018) 15.

[40] X. Ran, Z. Ye, M. Fu, Q. Wang, H. Wu, S. Lin, T. Yin, T. Hu, G. Wang, Design, Preparation, and Performance of a Novel Bilayer Tissue-Engineered Small-Diameter Vascular Graft, *Macromol Biosci* 19(3) (2019) e1800189.

- [41] R.H. Liu, C.S. Ong, T. Fukunishi, K. Ong, N. Hibino, Review of Vascular Graft Studies in Large Animal Models, *Tissue Eng Part B Rev* 24(2) (2018) 133-143.
- [42] S. Lu, P. Zhang, X. Sun, F. Gong, S. Yang, L. Shen, Z. Huang, C. Wang, Synthetic ePTFE grafts coated with an anti-CD133 antibody-functionalized heparin/collagen multilayer with rapid in vivo endothelialization properties, *ACS Appl Mater Interfaces* 5(15) (2013) 7360-9.
- [43] O.F. Khan, M.V. Sefton, Endothelialized biomaterials for tissue engineering applications in vivo, *Trends in Biotechnology* 29(8) (2011) 379-387.
- [44] K. Liu, N. Wang, W. Wang, L. Shi, H. Li, F. Guo, L. Zhang, L. Kong, S. Wang, Y. Zhao, A bio-inspired high strength three-layer nanofiber vascular graft with structure guided cell growth, *Journal of Materials Chemistry B* 5(20) (2017) 3758-3764.
- [45] Y. Yao, J. Wang, Y. Cui, R. Xu, Z. Wang, J. Zhang, K. Wang, Y. Li, Q. Zhao, D. Kong, Effect of sustained heparin release from PCL/chitosan hybrid small-diameter vascular grafts on anti-thrombogenic property and endothelialization, *Acta Biomater* 10(6) (2014) 2739-49.
- [46] L. Bai, J. Zhao, Q. Li, J. Guo, X. Ren, S. Xia, W. Zhang, Y. Feng, Biofunctionalized Electrospun PCL-PIBMD/SF Vascular Grafts with PEG and Cell-Adhesive Peptides for Endothelialization, *Macromol Biosci* 19(2) (2019) e1800386.

- [47] J. Shi, S. Chen, L. Wang, X. Zhang, J. Gao, L. Jiang, D. Tang, L. Zhang, A. Midgley, D. Kong, S. Wang, Rapid endothelialization and controlled smooth muscle regeneration by electrospun heparin-loaded polycaprolactone/gelatin hybrid vascular grafts, *J Biomed Mater Res B Appl Biomater* 107(6) (2019) 2040-2049.
- [48] R. Johnson, Y. Ding, N. Nagiah, E. Monnet, W. Tan, Coaxially-structured fibres with tailored material properties for vascular graft implant, *Materials Science and Engineering: C* 97 (2019) 1-11.
- [49] T. Fukunishi, C.A. Best, T. Sugiura, T. Shoji, T. Yi, B. Udelsman, D. Ohst, C.S. Ong, H. Zhang, T. Shinoka, C.K. Breuer, J. Johnson, N. Hibino, Tissue-Engineered Small Diameter Arterial Vascular Grafts from Cell-Free Nanofiber PCL/Chitosan Scaffolds in a Sheep Model, *PLOS ONE* 11(7) (2016) e0158555.
- [50] Z. Wang, Y. Wu, J. Wang, C. Zhang, H. Yan, M. Zhu, K. Wang, C. Li, Q. Xu, D. Kong, Effect of Resveratrol on Modulation of Endothelial Cells and Macrophages for Rapid Vascular Regeneration from Electrospun Poly(ϵ -caprolactone) Scaffolds, *ACS Applied Materials & Interfaces* 9(23) (2017) 19541-19551.
- [51] K.T. Shalumon, S. Deepthi, M.S. Anupama, S.V. Nair, R. Jayakumar, K.P. Chennazhi, Fabrication of poly (l-lactic acid)/gelatin composite tubular scaffolds for vascular tissue engineering, *International Journal of Biological Macromolecules* 72 (2015) 1048-1055.
- [52] X. Li, X. Wang, D. Yao, J. Jiang, X. Guo, Y. Gao, Q. Li, C. Shen, Effects of aligned and random fibers with different diameter on cell behaviors, *Colloids and Surfaces B: Biointerfaces* 171 (2018) 461-467.

- [53] Z. Tan, X. Gao, T. Liu, Y. Yang, J. Zhong, C. Tong, Y. Tan, Electrospun vein grafts with high cell infiltration for vascular tissue engineering, *Mater Sci Eng C Mater Biol Appl* 81 (2017) 407-415.
- [54] C. Vaz, S. Van Tuijl, C. Bouten, F. Baaijens, Design of scaffolds for blood vessel tissue engineering using a multi-layering electrospinning technique, *Acta biomaterialia* 1(5) (2005) 575-582.
- [55] J. Venugopal, L.L. Ma, T. Yong, S. Ramakrishna, In vitro study of smooth muscle cells on polycaprolactone and collagen nanofibrous matrices, *Cell Biol Int* 29(10) (2005) 861-7.
- [56] A. Chanda, J. Adhikari, A. Ghosh, S.R. Chowdhury, S. Thomas, P. Datta, P. Saha, Electrospun chitosan/polycaprolactone-hyaluronic acid bilayered scaffold for potential wound healing applications, *International journal of biological macromolecules* 116 (2018) 774-785.
- [57] U. Bertram, D. Steiner, B. Poppitz, D. Dippold, K. Köhn, J.P. Beier, R. Detsch, A.R. Boccaccini, D.W. Schubert, R.E. Horch, A. Arkudas, Vascular Tissue Engineering: Effects of Integrating Collagen into a PCL Based Nanofiber Material, *BioMed Research International* 2017 (2017) 9616939.
- [58] W.-Y. Choi, H.-E. Kim, M.-J. Kim, U.-C. Kim, J.-H. Kim, Y.-H. Koh, Production and characterization of calcium phosphate (CaP) whisker-reinforced poly (ϵ -caprolactone) composites as bone regenerative, *Materials Science and Engineering: C* 30(8) (2010) 1280-1284.
- [59] B. Lei, K.-H. Shin, D.-Y. Noh, I.-H. Jo, Y.-H. Koh, H.-E. Kim, S.E. Kim, Sol-gel derived nanoscale bioactive glass (NBG) particles reinforced poly (ϵ -

caprolactone) composites for bone tissue engineering, *Materials Science and Engineering: C* 33(3) (2013) 1102-1108.

[60] W.-Y. Choi, H.-E. Kim, Y.-H. Koh, Production, mechanical properties and in vitro biocompatibility of highly aligned porous poly (ϵ -caprolactone)(PCL)/hydroxyapatite (HA) scaffolds, *Journal of Porous Materials* 20(4) (2013) 701-708.

[61] T.-S. Jang, E.-J. Lee, J.-H. Jo, J.-M. Jeon, M.-Y. Kim, H.-E. Kim, Y.-H. Koh, Fibrous membrane of nano-hybrid poly-L-lactic acid/silica xerogel for guided bone regeneration, *Journal of Biomedical Materials Research Part B: Applied Biomaterials* 100B(2) (2012) 321-330.

[62] E.-J. Lee, S.-H. Teng, T.-S. Jang, P. Wang, S.-W. Yook, H.-E. Kim, Y.-H. Koh, Nanostructured poly (ϵ -caprolactone)–silica xerogel fibrous membrane for guided bone regeneration, *Acta biomaterialia* 6(9) (2010) 3557-3565.

[63] Z.C. Chen, A.K. Ekaputra, K. Gauthaman, P.G. Adaikan, H. Yu, D.W. Huttmacher, In vitro and in vivo analysis of co-electrospun scaffolds made of medical grade poly(epsilon-caprolactone) and porcine collagen, *J Biomater Sci Polym Ed* 19(5) (2008) 693-707.

[64] C. Ayres, G.L. Bowlin, S.C. Henderson, L. Taylor, J. Shultz, J. Alexander, T.A. Telemeco, D.G. Simpson, Modulation of anisotropy in electrospun tissue-engineering scaffolds: Analysis of fiber alignment by the fast Fourier transform, *Biomaterials* 27(32) (2006) 5524-5534.

[65] C.P. Ng, M.A. Swartz, Mechanisms of interstitial flow-induced remodeling of fibroblast-collagen cultures, *Ann Biomed Eng* 34(3) (2006) 446-54.

- [66] C.P. Ng, B. Hinz, M.A. Swartz, Interstitial fluid flow induces myofibroblast differentiation and collagen alignment in vitro, *J Cell Sci* 118(Pt 20) (2005) 4731-9.
- [67] S. Gautam, C.-F. Chou, A.K. Dinda, P.D. Potdar, N.C. Mishra, Surface modification of nanofibrous polycaprolactone/gelatin composite scaffold by collagen type I grafting for skin tissue engineering, *Materials Science and Engineering: C* 34 (2014) 402-409.
- [68] B. Li, S. Pan, H. Yuan, Y. Zhang, Optical and mechanical anisotropies of aligned electrospun nanofibers reinforced transparent PMMA nanocomposites, *Composites Part A: Applied Science and Manufacturing* 90 (2016) 380-389.
- [69] K. Madhavan, W.H. Elliott, W. Bonani, E. Monnet, W. Tan, Mechanical and biocompatible characterizations of a readily available multilayer vascular graft, *J Biomed Mater Res B Appl Biomater* 101(4) (2013) 506-19.
- [70] J. Tang, L. Bao, X. Li, L. Chen, F.F. Hong, Potential of PVA-doped bacterial nano-cellulose tubular composites for artificial blood vessels, *Journal of Materials Chemistry B* 3(43) (2015) 8537-8547.
- [71] C.J. van Andel, P.V. Pistecky, C. Borst, Mechanical properties of porcine and human arteries: implications for coronary anastomotic connectors, *Ann Thorac Surg* 76(1) (2003) 58-64; discussion 64-5.
- [72] Z. Wang, Y. Cui, J. Wang, X. Yang, Y. Wu, K. Wang, X. Gao, D. Li, Y. Li, X.L. Zheng, Y. Zhu, D. Kong, Q. Zhao, The effect of thick fibers and large pores of electrospun poly(epsilon-caprolactone) vascular grafts on macrophage polarization and arterial regeneration, *Biomaterials* 35(22) (2014) 5700-10.

- [73] F.J. Chaparro, M.E. Matusicky, M.J. Allen, J.J. Lannutti, Biomimetic microstructural reorganization during suture retention strength evaluation of electrospun vascular scaffolds, *Journal of Biomedical Materials Research Part B: Applied Biomaterials* 104(8) (2016) 1525-1534.
- [74] A.K. Gaharwar, M. Nikkhah, S. Sant, A. Khademhosseini, Anisotropic poly (glycerol sebacate)-poly (ϵ -caprolactone) electrospun fibers promote endothelial cell guidance, *Biofabrication* 7(1) (2014) 015001-015001.
- [75] P.F. Sánchez, E.M. Brey, J.C. Briceño, Endothelialization mechanisms in vascular grafts, *Journal of Tissue Engineering and Regenerative Medicine* 12(11) (2018) 2164-2178.
- [76] J.U. Park, H.D. Jung, E.H. Song, T.H. Choi, H.E. Kim, J. Song, S. Kim, The accelerating effect of chitosan-silica hybrid dressing materials on the early phase of wound healing, *J Biomed Mater Res B Appl Biomater* 105(7) (2017) 1828-1839.
- [77] E.H. Song, S.H. Jeong, J.U. Park, S. Kim, H.E. Kim, J. Song, Polyurethane-silica hybrid foams from a one-step foaming reaction, coupled with a sol-gel process, for enhanced wound healing, *Mater Sci Eng C Mater Biol Appl* 79 (2017) 866-874.
- [78] J.U. Park, S.H. Jeong, E.H. Song, J. Song, H.E. Kim, S. Kim, Acceleration of the healing process of full-thickness wounds using hydrophilic chitosan-silica hybrid sponge in a porcine model, *J Biomater Appl* 32(8) (2018) 1011-1023.

- [79] J.Y. Choi, M.Y. Shin, S.H. Suh, S. Park, Lyso-globotriaosylceramide downregulates KCa3.1 channel expression to inhibit collagen synthesis in fibroblasts, *Biochem Biophys Res Commun* 468(4) (2015) 883-8.
- [80] G. Arcangeli, V. Cupelli, G. Giuliano, Effects of silica on human lung fibroblast in culture, *Science of The Total Environment* 270(1) (2001) 135-139.
- [81] D.M. Martin, F.J. Boyle, Drug-eluting stents for coronary artery disease: A review, *Medical Engineering & Physics* 33(2) (2011) 148-163.
- [82] T.S. Jang, J.H. Lee, S. Kim, C. Park, J. Song, H.J. Jae, H.E. Kim, J.W. Chung, H.D. Jung, Ta ion implanted nanoridge-platform for enhanced vascular responses, *Biomaterials* 223 (2019) 119461.
- [83] M.H. Kang, K.H. Cheon, K.I. Jo, J.H. Ahn, H.E. Kim, H.D. Jung, T.S. Jang, An asymmetric surface coating strategy for improved corrosion resistance and vascular compatibility of magnesium alloy stents, *Mater Design* 196 (2020).
- [84] C. Park, S. Kim, H.E. Kim, T.S. Jang, Mechanically stable tantalum coating on a nano-roughened NiTi stent for enhanced radiopacity and biocompatibility, *Surf Coat Tech* 305 (2016) 139-145.
- [85] S. Borhani, S. Hassanajili, S.H. Ahmadi Tafti, S. Rabbani, Cardiovascular stents: overview, evolution, and next generation, *Prog Biomater* 7(3) (2018) 175-205.
- [86] B. Tesfamariam, Bioresorbable vascular scaffolds: Biodegradation, drug delivery and vascular remodeling, *Pharmacological Research* 107 (2016) 163-171.

- [87] G. Rebagay, S. Bangalore, Biodegradable Polymers and Stents: the Next Generation?, *Current Cardiovascular Risk Reports* 13(8) (2019).
- [88] D. Hoare, A. Bussooa, S. Neale, N. Mirzai, J. Mercer, The Future of Cardiovascular Stents: Bioresorbable and Integrated Biosensor Technology, *Adv Sci (Weinh)* 6(20) (2019) 1900856.
- [89] T.Ø. Barkholt, B. Webber, N.R. Holm, J.A. Ormiston, Mechanical properties of the drug-eluting bioresorbable magnesium scaffold compared with polymeric scaffolds and a permanent metallic drug-eluting stent, *Catheterization and Cardiovascular Interventions* (2019).
- [90] H.-S. Han, S. Loffredo, I. Jun, J. Edwards, Y.-C. Kim, H.-K. Seok, F. Witte, D. Mantovani, S. Glyn-Jones, Current status and outlook on the clinical translation of biodegradable metals, *Materials Today* 23 (2019) 57-71.
- [91] P. Severino, L. Netti, M.V. Mariani, A. Maraone, A. D'Amato, R. Scarpati, F. Infusino, M. Pucci, C. Lavalle, V. Maestrini, M. Mancone, F. Fedele, Prevention of Cardiovascular Disease: Screening for Magnesium Deficiency, *Cardiol Res Pract* 2019 (2019) 4874921.
- [92] D. Zhu, J. You, N. Zhao, H. Xu, Magnesium Regulates Endothelial Barrier Functions through TRPM7, MagT1, and S1P1, *Adv Sci (Weinh)* 6(18) (2019) 1901166.
- [93] M. Shahin, K. Munir, C. Wen, Y. Li, Magnesium matrix nanocomposites for orthopedic applications: A review from mechanical, corrosion, and biological perspectives, *Acta Biomaterialia* 96 (2019) 1-19.

- [94] L. Mao, L. Shen, J. Chen, X. Zhang, M. Kwak, Y. Wu, R. Fan, L. Zhang, J. Pei, G. Yuan, C. Song, J. Ge, W. Ding, A promising biodegradable magnesium alloy suitable for clinical vascular stent application, *Sci Rep* 7 (2017) 46343.
- [95] S.K. Yazdani, A. Sheehy, S. Pacetti, B. Rittlemeier, F.D. Kolodgie, R. Virmani, Stent Coating Integrity of Durable and Biodegradable Coated Drug Eluting Stents, *Journal of Interventional Cardiology* 29(5) (2016) 483-490.
- [96] S.-H. Ye, Y. Chen, Z. Mao, X. Gu, V. Shankarraman, Y. Hong, V. Shanov, W.R. Wagner, Biodegradable Zwitterionic Polymer Coatings for Magnesium Alloy Stents, *Langmuir* 35(5) (2019) 1421-1429.
- [97] T. Hu, C. Yang, S. Lin, Q. Yu, G. Wang, Biodegradable stents for coronary artery disease treatment: Recent advances and future perspectives, *Materials Science and Engineering C* 91 (2018) 163-178.
- [98] W. Jiang, Q. Tian, T. Vuong, M. Shashaty, C. Gopez, T. Sanders, H. Liu, Comparison Study on Four Biodegradable Polymer Coatings for Controlling Magnesium Degradation and Human Endothelial Cell Adhesion and Spreading, *ACS Biomaterials Science & Engineering* 3(6) (2017) 936-950.
- [99] A. Witecka, A. Yamamoto, J. Idaszek, A. Chlanda, W. Świąszkowski, Influence of biodegradable polymer coatings on corrosion, cytocompatibility and cell functionality of Mg-2.0Zn-0.98Mn magnesium alloy, *Colloids and Surfaces B: Biointerfaces* 144 (2016) 284-292.
- [100] O. Nikoubashman, S. Heringer, K. Feher, M.-A. Brockmann, B. Sellhaus, A. Dreser, K. Kurtenbach, R. Pjontek, S. Jockenhövel, J. Weis, F. Kießling, T. Gries, M. Wiesmann, Development of a Polymer-Based Biodegradable

Neurovascular Stent Prototype: A Preliminary In Vitro and In Vivo Study, *Macromolecular Bioscience* 18(7) (2018) 1700292.

[101] I.H. Bae, M.H. Jeong, K.S. Lim, D.S. Park, J.W. Shim, J.K. Park, K.H. Oh, M.R. Jin, D.S. Sim, Novel Polymer-Free Everolimus-Eluting Stent Fabricated using Femtosecond Laser Improves Re-endothelialization and Anti-inflammation, *Sci Rep* 8(1) (2018) 7383.

[102] H.M. Mousa, A. Abdal-hay, M. Bartnikowski, I.M.A. Mohamed, A.S. Yasin, S. Ivanovski, C.H. Park, C.S. Kim, A Multifunctional Zinc Oxide/Poly(Lactic Acid) Nanocomposite Layer Coated on Magnesium Alloys for Controlled Degradation and Antibacterial Function, *ACS Biomaterials Science & Engineering* 4(6) (2018) 2169-2180.

[103] R.S. El-Kamel, A.A. Ghoneim, A.M. Fekry, Electrochemical, biodegradation and cytotoxicity of graphene oxide nanoparticles/polythreonine as a novel nano-coating on AZ91E Mg alloy staple in gastrectomy surgery, *Materials Science and Engineering: C* 103 (2019) 109780.

[104] S. Sharifi Golru, M.M. Attar, B. Ramezanzadeh, Studying the influence of nano-Al₂O₃ particles on the corrosion performance and hydrolytic degradation resistance of an epoxy/polyamide coating on AA-1050, *Progress in Organic Coatings* 77(9) (2014) 1391-1399.

[105] L. Ejenstam, A. Swerin, J. Pan, P.M. Claesson, Corrosion protection by hydrophobic silica particle-polydimethylsiloxane composite coatings, *Corrosion Science* 99 (2015) 89-97.

- [106] S. Park, J. Kim, M.K. Lee, C. Park, H.D. Jung, H.E. Kim, T.S. Jang, Fabrication of strong, bioactive vascular grafts with PCL/collagen and PCL/silica bilayers for small-diameter vascular applications, *Materials & Design* 181 (2019).
- [107] T.S. Jang, K.H. Cheon, J.H. Ahn, E.H. Song, H.E. Kim, H.D. Jung, In-vitro blood and vascular compatibility of sirolimus-eluting organic/inorganic hybrid stent coatings, *Colloid Surface B* 179 (2019) 405-413.
- [108] U. Eduok, J. Szpunar, Bioinspired and hydrophobic alkyl-silanized protective polymer coating for Mg alloy, *Prog Nat Sci-Mater* 28(3) (2018) 354-362.
- [109] W. Yang, Y. Zhong, C. He, S. Peng, Y. Yang, F. Qi, P. Feng, C. Shuai, Electrostatic self-assembly of pFe₃O₄ nanoparticles on graphene oxide: A co-dispersed nanosystem reinforces PLLA scaffolds, *Journal of Advanced Research* 24 (2020) 191-203.
- [110] C. Shuai, X. Yuan, W. Yang, S. Peng, G. Qian, Z. Zhao, Synthesis of a mace-like cellulose nanocrystal@Ag nanosystem via in-situ growth for antibacterial activities of poly-L-lactide scaffold, *Carbohydrate Polymers* 262 (2021) 117937.
- [111] W. Stöber, A. Fink, E. Bohn, Controlled growth of monodisperse silica spheres in the micron size range, *Journal of Colloid and Interface Science* 26(1) (1968) 62-69.
- [112] Y. Yang, C. He, E. Dianyu, W. Yang, F. Qi, D. Xie, L. Shen, S. Peng, C. Shuai, Mg bone implant: Features, developments and perspectives, *Materials*

& Design 185 (2020) 108259.

[113] Y.J. Shi, J. Pei, J. Zhang, J.L. Niu, H. Zhang, S.R. Guo, Z.H. Li, G.Y. Yuan, Enhanced corrosion resistance and cytocompatibility of biodegradable Mg alloys by introduction of $\text{Mg}(\text{OH})_2$ particles into poly (L-lactic acid) coating, *Sci Rep* 7 (2017) 41796.

[114] Y. Sun, Z. Zhang, C.P. Wong, Study on mono-dispersed nano-size silica by surface modification for underfill applications, *J Colloid Interface Sci* 292(2) (2005) 436-44.

[115] H. Gu, Q. Zhang, J. Gu, N. Li, J. Xiong, Facile preparation of superhydrophobic silica nanoparticles by hydrothermal-assisted sol-gel process and effects of hydrothermal time on surface modification, *Journal of Sol-Gel Science and Technology* 87(2) (2018) 478-485.

[116] H. Liu, T.J. Webster, Mechanical properties of dispersed ceramic nanoparticles in polymer composites for orthopedic applications, *International Journal of Nanomedicine* 5 (2010) 299-313.

[117] Z. Sekhavat Pour, M. Ghaemy, S. Bordbar, H. Karimi-Maleh, Effects of surface treatment of TiO_2 nanoparticles on the adhesion and anticorrosion properties of the epoxy coating on mild steel using electrochemical technique, *Progress in Organic Coatings* 119 (2018) 99-108.

[118] W. Zhang, Y. Chen, M. Chen, S. Zhao, J. Mao, A. Qu, W. Li, Y. Zhao, N. Huang, G. Wan, Strengthened corrosion control of poly (lactic acid) (PLA) and poly (ϵ -caprolactone) (PCL) polymer-coated magnesium by imbedded hydrophobic stearic acid (SA) thin layer, *Corrosion Science* 112 (2016) 327-

337.

[119] Y.Y. Gao, J. Liu, J.X. Shen, L.Q. Zhang, Z.H. Guo, D.P. Cao, Uniaxial deformation of nanorod filled polymer nanocomposites: a coarse-grained molecular dynamics simulation, *Phys Chem Chem Phys* 16(30) (2014) 16039-16048.

[120] M. El Achaby, N. El Miri, A. Aboulkas, M. Zahouily, E. Bilal, A. Barakat, A. Solhy, Processing and properties of eco-friendly bio-nanocomposite films filled with cellulose nanocrystals from sugarcane bagasse, *International Journal of Biological Macromolecules* 96 (2017) 340-352.

[121] R.A. Riggleman, G. Toepperwein, G.J. Papakonstantopoulos, J.L. Barrat, J.J. de Pablo, Entanglement network in nanoparticle reinforced polymers, *J Chem Phys* 130(24) (2009) 244903.

[122] J.-L. Tsai, H. Hsiao, Y.-L. Cheng, Investigating Mechanical Behaviors of Silica Nanoparticle Reinforced Composites, *Journal of Composite Materials* 44(4) (2010) 505-524.

[123] D.-J. Kwon, P.-S. Shin, J.-H. Kim, Y.-M. Baek, H.-S. Park, K.L. DeVries, J.-M. Park, Interfacial properties and thermal aging of glass fiber/epoxy composites reinforced with SiC and SiO₂ nanoparticles, *Composites Part B: Engineering* 130 (2017) 46-53.

[124] Y. Yang, Y. Cheng, S. Peng, L. Xu, C. He, F. Qi, M. Zhao, C. Shuai, Microstructure evolution and texture tailoring of reduced graphene oxide reinforced Zn scaffold, *Bioactive Materials* 6(5) (2021) 1230-1241.

[125] B. Zhang, R. Yao, M.F. Maitz, G. Mao, Z. Hou, H. Yu, R. Luo, Y. Wang, Poly (dimethyl diallyl ammonium chloride) incorporated multilayer coating on biodegradable AZ31 magnesium alloy with enhanced resistance to chloride corrosion and promoted endothelialization, *Chemical Engineering Journal* (2020) 127724.

[126] N.J. Ostrowski, B. Lee, A. Roy, M. Ramanathan, P.N. Kumta, Biodegradable poly(lactide-co-glycolide) coatings on magnesium alloys for orthopedic applications, *Journal of Materials Science: Materials in Medicine* 24(1) (2013) 85-96.

[127] Y. Zhu, L. Zheng, W. Liu, L. Qin, T. Ngai, Poly(l-lactic acid) (PLLA)/MgSO₄·7H₂O Composite Coating on Magnesium Substrates for Corrosion Protection and Cytocompatibility Promotion, *ACS Applied Bio Materials* 3(3) (2020) 1364-1373.

[128] J. Xie, J. Hu, X. Lin, L. Fang, F. Wu, X. Liao, H. Luo, L. Shi, Robust and anti-corrosive PDMS/SiO₂ superhydrophobic coatings fabricated on magnesium alloys with different-sized SiO₂ nanoparticles, *Applied Surface Science* 457 (2018) 870-880.

[129] I.O. Arukalam, E.E. Oguzie, Y. Li, Fabrication of FDTs-modified PDMS-ZnO nanocomposite hydrophobic coating with anti-fouling capability for corrosion protection of Q235 steel, *Journal of Colloid and Interface Science* 484 (2016) 220-228.

[130] M. Ganjaee Sari, M. Shamshiri, B. Ramezanzadeh, Fabricating an epoxy composite coating with enhanced corrosion resistance through impregnation of functionalized graphene oxide-co-montmorillonite Nanoplatelet, *Corrosion*

Science 129 (2017) 38-53.

[131] S.M. Oliveira, N.M. Alves, J.F. Mano, Cell interactions with superhydrophilic and superhydrophobic surfaces, *Journal of Adhesion Science and Technology* 28(8-9) (2014) 843-863.

[132] M. Ferrari, F. Cirisano, M.C. Morán, Mammalian Cell Behavior on Hydrophobic Substrates: Influence of Surface Properties, *Colloids and Interfaces* 3(2) (2019) 48.

[133] J.G. Croissant, Y. Fatieiev, N.M. Khashab, Degradability and Clearance of Silicon, Organosilica, Silsesquioxane, Silica Mixed Oxide, and Mesoporous Silica Nanoparticles, *Adv Mater* 29(9) (2017).

[134] T. Govindarajan, R. Shandas, Shape Memory Polymers Containing Higher Acrylate Content Display Increased Endothelial Cell Attachment, *Polymers* 9(11) (2017) 572.

[135] T.-W. Chung, D.-Z. Liu, S.-Y. Wang, S.-S. Wang, Enhancement of the growth of human endothelial cells by surface roughness at nanometer scale, *Biomaterials* 24(25) (2003) 4655-4661.

Abstract (Korean)

국문 초록

기계적 특성 및 혈관내피화 속도가 향상된

혈관조직공학용 고분자/실리카 복합체

서울대학교 공과대학

재료공학부

박 수 형

심혈관계 질환 발병률과 사망률이 증가함에 따라 생분해성 혈관 임플란트의 수요가 점진적으로 늘어나고 있다. 생분해성 재료는 이식 부위의 조직이 수복됨과 동시에 서서히 분해된다. 이는 기존의 혈관 임플란트가 체내에 영구적으로 잔존함으로 인해 빈번하게 발생하는 혈전 형성이나 혈관 재협착 등의 부작용을 줄여줄 수 있다. 일반적으로 고분자 재료는 유연하고 가공이 용이하여 혈관 임

플라트 재료로서 각광받고 있지만, 생체 적합성 (biocompatibility) 과 물리적 기능성이 부족하여 임상 사용에 제한이 있다. 이를 향상하고자 생체 활성 세라믹 재료와 복합체(composite)로 제작하는 연구가 활발하게 진행되고 있으며, 이때 복합체의 재료 및 구조에 변화를 주어 고분자와 세라믹이 서로 상호보완 가능토록 하였다. 대표적인 생체 활성 세라믹 재료인 실리카는 체내에서 가수분해되어 조직의 재생과 혈관 재형성(angiogenesis)을 촉진할 수 있을 뿐 아니라, 합성 시 실리카 전구체의 농도, 반응 시간, 혹은 pH 조건 등을 조절하면 다양한 형상으로 제작할 수 있다는 장점이 있다. 따라서 본 연구에서는 고분자/실리카 복합체가 혈관 임플란트의 적용 부위에 따라 달리 요구되는 물리적 기능성을 갖도록 구성하여 제작하였다.

첫 번째 연구에서는 전기방사법을 이용하여 이중층 구조의 나노 섬유 멤브레인 인공 혈관을 제작하였다. 의료용 고분자 소재인 폴리카프로락톤(PCL)을 주재료로 하였으며, 외벽은 임의배열된 PCL/실리카제로젤 복합체로, 내벽은 일축배열된 PCL/콜라겐 복합체로 구성하여, 기존 단일 고분자가 지니는 한계점을 극복하였다. 내경이 6 mm 이하인 소구경 인공 혈관의 경우, 실제 혈관과 유사한 인장 강도, 봉합 견고성과 항혈전성(anti-thrombogenicity)을 가져야 장기간 개통성(patency)을 유지할 수 있다. 본 연구에선 실제 사람 혈관의 구조와 기능을 모사하여, 혈류에 따른 동적 유압 응력을 견딜 수 있도록, 높은 혈액 적합성(hemocompatibility)을 지니도록

록 하였다. 먼저 외벽 제작 시, 산 촉매 하에서 실리카 전구체를 반응시켜, 나노골격구조의 실리카제로젤이 PCL 섬유 전반에 걸쳐 존재하도록 하였고, 이는 주변 조직 세포와 친화적이면서도 높은 기계적 강도를 지녔다. 또한 외벽의 안쪽에 얇은 PCL/콜라겐 복합체 섬유를 혈류와 평행한 방향으로 배열시켜, 혈관내피세포(endothelial cell)가 부착, 이동, 증식하기 용이하도록 하였고, 이는 곧 빠른 혈관내피화(rapid endothelialization)를 의미한다. 따라서 본 연구에서 고안한 전기방사 PCL 기반의 이중층 인공 혈관은 빠른 혈관내피세포 커버리지(coverage)와 충분한 기계적 물성을 지녀 혈관 이식 수술 시 발생 가능한 혈전증(luminal thrombosis) 및 내막 과증식(intimal hyperplasia)을 최소화할 것으로 예상된다.

두 번째 연구에서는 생분해성 마그네슘 스텐트의 부식 저항성과 생체 활성을 증진시키기 위하여 기존의 폴리락티드(PLLA) 코팅층에 표면 처리한 실리카 나노 입자를 균일하게 혼재 시켰다. 마그네슘 스텐트는 좁아진 혈관 내벽을 지지하기에 충분한 강도를 지녔을 뿐 아니라, 면역 반응 및 독성이 없는 재료이지만, 생리학적 환경에서 높은 반응성으로 인하여 사용에 제약이 있다. 마그네슘 스텐트 코팅층 재료로는, 팽창-수축 과정에서도 안정적인, 유연한 고분자 소재가 주로 사용되지만, 단일 고분자 코팅층으로선 부식을 막기에 충분하지 못하고 생체 적합성도 낮다는 한계가 있다. 따라서 본 연구에선 염기 촉매 하에서 실리카 전구체를 가수분해 하여 실리카 나노 입자를 성장시키고, 이를 연속적으로 헥사데실트리메톡시

실레인(hexadecyltrimethoxysilane)과 반응시켜 나노 입자 표면에 긴 알킬기($-(CH_2)_{15}CH_3$)가 노출되도록 표면 개질 하였다. 이를 통해 상대적 소수성 고분자인 PLLA 모재 내에서 나노 입자가 뭉침 없이 균일하게 분산되도록 하였으며, 나노 입자의 소수성 표면은 복합체 코팅층의 부식 저항성 역시 향상시켰다. 즉, 실리카 나노 입자는 물 분자가 침투하여 마그네슘 기판을 부식시키는 과정을 물리적으로 방해할 뿐 아니라, 체내에서 실리콘 이온을 방출하여 혈관내피세포를 자극하는 생체 활성 물질로도 작용한다. 특히 10 wt%와 20 wt%의 실리카 나노 입자를 함유하는 복합체 코팅층은 기존의 단일 고분자 코팅층 대비, 마그네슘의 부식 속도를 반 이상 감소시키고, 혈관내피세포와의 친화성이 매우 우수하였다.

상기 연구 결과들을 종합해 보았을 때, 생체 활성 세라믹 재료인 실리카는 솔젤법을 통해 다양한 구조의 고분자/실리카 복합체를 형성할 수 있으며, 이를 혈관 임플란트에 적용하면 안정적으로 혈관 재형성을 촉진할 수 있음을 입증하였다. 생분해성 고분자/실리카 복합체는 체내에서 분해되면서 섬유아세포와 혈관내피세포를 자극하여, 우수한 생체 기능성을 나타낸다. 또한 나노골격구조의 실리카제로젤은 고분자의 기계적 강도를 증진시키고, 소수성으로 개질된 실리카 나노 입자는 고분자 코팅층의 부식 저항성을 증진시켰으며, 이는 복합체의 물리적 기능성을 의미한다. 즉, 본 연구에서 소개한 고분자/실리카 복합체는 높은 생체 적합성과 함께, 다양한 혈관 임플란트에서 요구되는 물리적 기능성 역시 지닐 수 있음을 확인하

였다.

주요어(Keywords): 혈관 조직 공학, 고분자 임플란트, 실리카, 고분자/실리카 복합체, 나노 복합체, 생체 활성

학번: 2017-26470

감사의 글 (Acknowledgement)

2012년 3월, 어른 아닌 어른의 모습으로 서울대학교에 입학했습니다. 모든 게 새롭고 재미있어서 느슨하게 살았고, 1학년 2학기에 첫 번째 전공수업을 듣고선 ‘내가 전공을 잘못 선택했나?’하며 그동안 열심히 하지 않은 걸 애써 부정하기도 했었습니다. 이제는 캠퍼스 어디를 둘러봐도 추억이 묻어 있는 것 같습니다. 날씨 좋은 날 버들골에서 영문학 야외 수업을 한 적이 있었는데, 심오하고 어려운 와중에 분위기에 취해 마냥 행복했던 기억이 납니다. 물리 시험을 마치고 나니 폭설이 내려 다 같이 정문까지 걸어내려 갔던 것도, 아침 일찍 열역학 시험이 있어서 친구들과 도서관에서 날을 새고 시험을 봤던 것도, 다 정말 소중한 추억들입니다. 이제 근 10년간의 관악생활을 재료공학 박사라는, 작지만 분명한 마침표로서 마무리하게 되었습니다.

할머니, 부모님, 오빠의 아낌없는 사랑과 응원에 감사드립니다. 아직도 잠옷 차림으로 거실에 누워만 있어도 예쁘다고 해주시는 가족들의 사랑이 있었기에, 이렇게 정서적으로 건강하게 성장할 수 있었습니다. 늦은 나이에 검정고시로 공부를 끝마치시고 여전히 배움에 열정이 가득하신 할머니 덕분에, 자연스레 공부를 좋아했던 것 같습니다. 공주처럼 키워주시고, 훌륭한 사람이 되라고 응원해 주신 우리 할머니, 사랑합니다. 언제나 딸의 행복을 최우선으로 여기시고 제 선택을 믿고 격려해 주신 부모님께도 정말 감사합니다. 느리게

살아도 괜찮다고, 하루 한 번은 하늘을 올려다보는 여유를 가지라는
아빠의 말씀, 힘들 때마다 상기하며 마음을 다잡겠습니다. 제가 늦
게까지 공부하면 늘 같이 밤을 지새워 주시고, 밝고 따뜻한 사람으
로 키워주신 엄마, 엄마가 제 엄마라서 너무 행복합니다. 그리고 나
의 가장 소중한 단짝친구 우리 오빠, 가끔은 동등한 성인으로 존중
해 주고, 가끔은 열렬한 동생바보가 되어 응원해 줘서 정말 고맙습
니다. 형용할 수 없을 만큼의 사랑을 받아 보답할 자신조차 없지만,
적어도 그 큰 사랑, 늘 감사히 생각하겠습니다. 사랑합니다.

저의 지도교수님이신 김현이 교수님께 진심으로 감사드립니다.
다. 학부 때 교수님의 수업과 세미나를 듣고, 교수님의 인자하신 미
소와 생체 재료 분야에 이끌려 연구실에 들어오게 되었습니다. 부드
러우면서도 날카로운 조언으로 정도로 이끌어 주셨고, 제 마음을 꿰
뚫어 보시는 것처럼 당근과 채찍을 번갈아 주셔서 연구에 정진할
수 있었습니다. 실험이 잘 안되어 낙심했을 때면 함께 고민해 주시
고, 연구가 정체되어 있으면 교수님께서 더욱이 연구에 호기심을 드
러내시며 제가 다시 매진할 수 있도록 도와주셨습니다. 논문 때문에
슬펐다는 장난스러운 메일 한 줄에도, 많이 슬펐냐 물어봐 주시고
다독여 주신 교수님, 정말 감사합니다. 교수님의 따스함과 학문적
열정을 본받아, 교수님을 닮은 연구자로서 나아가겠습니다. 그리고
귀한 시간 내시어 저의 학위 논문을 지도하고 심사해 주신 안철희
교수님, 선정윤 교수님, 장태식 교수님, 정현도 교수님께도 진심으로
감사합니다. 다른 시각에서의 분석으로 전문적인 조언을 해주셔서,

한층 심도 있게 연구를 발전시킬 수 있었습니다. 그 간의 모든 연구를 함께 하며 세심하게 지도해 주신 장태식 교수님, 학문적인 지도 외에도, 연구자로서 깊이 고찰하는 자세를 가르쳐주셔서 정말 감사드리고 잊지 않겠습니다.

학위 과정 동안 연구실 생활을 함께 했던 모든 분들께 감사의 말씀을 드리고 싶습니다. 이성미 박사님과 현 · 호용 · 광희 · 다영 · 첸커 · 윤정 · 천일 · 은호 · 인구 · 경일 · 석우 · 진영 · 민규 선배, 그리고 10년 차 동기 창하에게 큰 감사를 드립니다. 실험 설계 방법과 구체적인 분석 방법을 하나하나 알려주고 활발히 의견을 주어, 성장할 수 있게 도와주셨습니다. 특히 천일 · 광희 선배와 함께 과제를 수행하고 비슷한 연구를 진행하면서, 영리하게 실험 계획을 세우는 법도, 꼼꼼하고 완벽하게 연구하는 법도, 논리적으로 연구를 풀어내는 법도, 연구과정에서 지치지 않는 법도, 참 많은 것을 배웠습니다. 그리고 퇴근길 만담을 나누며 저의 심리상담사를 자처한 인구 선배 덕분에, 힘들었던 날에도 즐겁게 퇴근할 수 있었습니다. 화목한 우리 연구실 사람들과 함께 했기에, 자칫 외로울 수 있는 학위 과정이 웃음으로 가득했습니다. 희로애락을 나누며 함께한 그 시간들은 저의 인생에 있어 중요한 순간으로 남을 것 같습니다.

제 곁의 모든 친구들에게 감사합니다. 온갖 군것질을 함께 해 준 학부동기 지용이와 학교 근처 맛집을 함께 섭렵한 동네친구 주연이에게 감사합니다. 먹는 즐거움도 컸지만, 서로 다른 분야의 연구 이야기도 공유하고 새로운 아이디어도 주고받는 과정에서의

지적 대화가 참 기억에 남습니다. 머리와 배가 동시에 풍족해지는 시간이었습니다. 뛰어난 지능과 훌륭한 인품을 가진, 여러 친구들이 어찌면 관악생활의 가장 큰 수확이라고 생각합니다. 모두가 저에게 정말 영향력 있는 사람이고, 활력과 자극을 주는 존재입니다. 각자의 위치에서 만족스러운 삶을 꾸리길 소원하고, 앞으로도 인연을 이어가고 싶습니다.

다시 한번 제가 학위를 받을 수 있도록 도와주신 모든 분들께 감사의 말씀을 드립니다. 언제나 건강하고 행복한 모습이길 바라겠습니다. 저의 연구 생활에 도움을 주신 많은 분들께 보답하는 마음으로, 발전하는 연구자가 되도록 노력하겠습니다. 그리고 저 역시도 나눌 수 있는 사람으로 성장해 나가겠습니다.

감사합니다.

2021년 7월 관악에서

박수형 올림